Nano-Structures & Nano-Objects 38 (2024) 101165

Contents lists available at ScienceDirect

Nano-Structures & Nano-Objects

journal homepage: www.elsevier.com/locate/nanoso

The role of Ga and Y on binary Al_2O_3-Y_2O_3 and Al_2O_3-Ga_2O_3 mixed oxides nanoparticles towards potential Ni water-gas shift catalysts

M.C. Ortiz-Domínguez [a,b], A. Solis-García [b], A.M. Venezia [c], S. Jimenez-Lam [d], S. Fuentes-Moyado [b], R. Ponce-Pérez [b], J. Guerrero-Sanchez [b], J.G. Pacheco-Sosa [a], J.N. Díaz de León [b,*]

[a] *División académica multidisciplinaria de Jalpa de Méndez, Universidad Juárez Autónoma de Tabasco, Carr. Estatal libre Villahermosa-Comalcalco, RIA. Rivera alta Jalpa de Méndez, Tabasco, Mexico*
[b] *Universidad Nacional Autónoma de México, Centro de Nanociencias y Nanotecnología México, Carretera Tijuana-Ensenada, Pedregal Playitas, Ensenada, B.C. 22860, México*
[c] *Instituto per lo Studio dei Material Nanostrutturati, Palermo 90146, Italy*
[d] *Facultad de Ciencias Químico Biológicas, Universidad Autónoma de Sinaloa, Josefa Ortiz de Domínguez, 80013, Ciudad Universitaria, Culiacán, Sinaloa, Mexico*

ARTICLE INFO

Keywords:
WGS
Mixed oxides
Urchin-like
Nanoparticles
XPS

ABSTRACT

This work focuses on the study of binary Al_2O_3-Y_2O_3-x and Al_2O_3-Ga_2O_3-x mixed oxides with varying Y_2O_3 or Ga_2O_3 nominal loading (x=25, 50) prepared by hydrothermal synthesis assisted by Triton X-100. The mixed oxides were used to prepare Ni-based (5 wt%) catalysts for the Water Gas Shift Reaction. The Al_2O_3 sample presented urchin-like hollow nanosphere morphology, which evolved to solid nanospheres with Y_2O_3 or Ga_2O_3 in the mixed oxides. The physicochemical characterization indicated good integration of the mixed oxides, especially on the low-content additive oxides. The theoretical results confirmed that Ga goes deeper into the alumina matrix than Y, partially explaining the XPS and HRTEM results in which the Ni dispersion was better in the Ni/AlGa-x samples. The FTIR in-situ measurements of the reaction allowed us to propose that the reaction occurs minimally through the carbonyl mechanism at low temperatures (<300 °C) and the formate mechanism at high temperatures (>300 °C).

1. Introduction

Greenhouse gases (GHG) like CO_2, CO, and methane could be used as raw materials to produce hydrocarbons sustainably. Besides this, the three GHG coexist in many industrial applications, i.e., the industrial hydrogen production from the water gas shift (WGS) reaction [1]. The carbon monoxide with steam is sent to the reformer along with some hydrocarbon in this process. When the C_nH_m hydrocarbon comes into contact with water in the presence of catalysts and high temperatures (~800°C), it forms CO and H_2, which also, depending on the contact time, can derive in methane [2]. Then, the reformer effluent is sent to the WGS reactors, which operate under lower temperature (400°C-500°C) conditions to thermodynamically shift the equilibrium to hydrogen production [2,3]. It is well known that several supported metals and metal oxides could catalyze this reaction. Early reports presented periodic trends of alumina-supported metals for the WGS reaction. Several metals of groups VIIB, VIII, and IB were analyzed, and the highest activity was presented by the Cu/Al_2O_3 sample [2]; this was explained in terms of the heat of adsorption for the carbon monoxide over Cu.

Materials with higher activities and compositions are industrially classified into four general groups: high and low-temperature WGS catalysts [3]. The high-temperature WGS (HTS) catalysts typically comprise around 74% of Fe_2O_3, 14% of Cr_2O_3, and 0.2% of MgO balance with volatile compounds [4]. These ferrochrome catalysts can operate in the range of 300°C to 450°C. Meanwhile, the low-temperature WGS (LTS) catalysts are prepared mainly with copper-zinc oxides and work between 190°C and 250°C [3]. The third type is sulfides based on cobalt and molybdenum, which are principally used when the stream carries some sulfur content, and they are called sour gas shift catalysts [5]. The fourth type is the middle-temperature WGS (MTS) catalysts, which in real terms are LTS or HTS catalysts modified with promoters or additives to work under these conditions. In this direction, the MTS catalysts are extensively studied using alumina as support and metals like Pt [6,7], Pd

---

* Corresponding author.
E-mail address: noejd@ens.cnyn.unam.mx (J.N. Díaz de León).

https://doi.org/10.1016/j.nanoso.2024.101165
Received 29 December 2023; Received in revised form 20 March 2024; Accepted 16 April 2024
Available online 30 April 2024

[7,8], Cu [9,10], and Ni [11,12] to improve activity and especially stability concerning the commonly used Cu/ZnO catalysts. However, several authors have reported that by using different redox-active supports, the mechanism of the WGS is modified entirely [9,10,13]. Supports made of pure metal oxides such as CeO_2 [9,14,15], ZrO_2 [16–18], and TiO_2[19] are extensively studied combined with Au, Ru, Rh Pt, Ag, and Cu [5]. Even mixed oxides like CeOx-TiO_2 [20], Cr_2O_3-Ga_2O_3[21], or Al_2O_3-Ga_2O_3 [7] have been tested with encouraging results. In that direction, our research group reported the effect of the binary Al_2O_3-Ga_2O_3 mixed oxide used as support of Os, Pd, Rh and Pt noble metals [7]. Each metal interacts differently with the AlGa support, even when all metal's charge and impregnation conditions are the same. The metal-support interactions lead to a wide range of dispersions; specifically, the Pt presented the smallest particles (Particle size = 0.6 ±0.1 nm) among the samples. Nevertheless, the more active material turned out to be the Pd/AlGa sample with 1.6±0.2 nm of Pd mean diameter. These results confirm that other factors, such as metal support interaction and oxygen availability, are crucial in the WGS reaction beyond dispersion [22].

In recent years, the increasing use of nanostructured particles or particles with nanoscale morphology has allowed the fine-tuning of the catalyst's properties for many applications such as hydrodesulfurization [23], CO_2 hydrogenation [24], dye degradation [25], alcohol transformation [26] and WGS reaction [15,27]. Nevertheless, we failed to find studies of nanoshaped materials such as solid nanospheres or urchin-like hollow nanospheres as supports of WGS catalysts. In recent work, we presented the effect of those morphologies for the catalytic dehydration of propanol using Al_2O_3-Y_2O_3 to prepare the nanoshaped catalysts [26]. Further than the good performance of the samples, it was noticed that the presence of Yttrium oxide induced an interesting interaction with alcohol, forming Y-CO bonds. At this point, it has to be mentioned that the effect of the presence of large quantities of Ga_2O_3 [28] or Y_2O_3 [26] in the mixed oxide considerably impacts the textural properties. Therefore, in this work, we focus on the effect of the binary Al_2O_3-Ga_2O_3 (AlGa-x) and Al_2O_3-Y_2O_3 (AlY-x) mixed oxides at concentrations equal to 50 wt% and below (with x=0, 25, 50, 100 wt% of the Ga_2O_3 or Y_2O_3) synthesized by hydrothermal method to obtain nanoshaped supports to prepare Ni (5 wt%) catalysts. Supports and catalysts will be widely characterized by X-ray diffraction (XRD), N_2 physisorption, scanning electron microscopy (SEM), Diffuse reflectance spectroscopy in ultraviolet-visible (DRS-UV–vis), temperature programmed reduction (TPR), temperature programmed ammonia desorption (TPD), transmission electron microscopy (TEM) and X-ray photoelectron spectroscopy (XPS). The WGS catalytic tests will be performed in a PID continuous flow microreactor and followed by in situ FTIR.

2. Materials and methods

2.1. Support synthesis

The Al_2O_3-Ga_2O_3 (AlGa-x) and Al_2O_3-Y_2O_3 (AlY-x) mixed oxides (with x=0, 25, 50, 100 wt% of the Ga_2O_3 or Y_2O_3) were prepared by the hydrothermal synthesis method developed for binary samples as reported in [26]. In this method, $Al_2(SO_4)_3$ was used as alumina precursor (Sigma Aldrich, 97%) mixed with different quantities of Ga $(NO_3)_3.8\,H_2O$ (Sigma Aldrich, 99.9%) or $Y(NO_3)_3.6\,H_2O$ (Sigma Aldrich, 99.8%) salts. Briefly, Triton-X100 was dissolved in deionized H_2O with vigorous stirring, then the amount of aluminum sulfate was added and kept in stirring for 30 minutes, then the chosen precursor i.e., gallium nitrate was added under stirring; finally, urea was added and kept in stirring during another 30 min. The resulting solution was placed in a Teflon-coated autoclave and thermally treated at 120 °C for 24 hours. A white precipitate was obtained, filtered, and washed with deionized water and ethanol anhydride 1:1. Finally, it was dried at 60 °C for 12 h and calcined at 550 °C for 6 h with a heating ramp of 10 $°C▪min^{-1}$. Each reactive amount was calculated to have the nominal weight percentage of Y_2O_3 or Ga_2O_3, maintaining the following molar proportion: 1:1.2:600:14 for metallic ions (Y, Ga, and Al), TX-100, water, and urea, respectively.

2.2. Catalysts preparation

For the catalyst, 5 wt% of Ni was loaded by the pore-filling method using nickel nitrate as a precursor ($Ni(NO_3)_2$-6 H_2O, Aldrich, ACS). In a typical preparation, the precursor was dissolved in the corresponding quantity of water, which agrees with the pore volume obtained from the measurement of the textural properties once the material is degasified. Then, 1 g of the corresponding support to be impregnated AlGa-(x) and AlY-(x) is added to the solution and mechanically mixed at room temperature. After reaching homogeneity, the wet powders were left to stand covered for 12 h and then dried uncovered in the laboratory fume hood with airflow for 12 hours. After that, the powders were dried in the oven under a static atmosphere at 120 °C for 4 hours and subsequently calcined at 450 °C for another four hours with a heating ramp of 5 $°C▪min^{-1}$.

2.3. Catalytic activity measurements

2.3.1. Activity test in a continuous flow microreactor

A twin PID continuous flow microreactor of stainless steel with a 0.9 cm inner diameter was used to perform the catalytic activity tests. Samples were in-situ reduced before the catalytic tests under 40 $cm^3▪min^{-1}$ of H_2 flow during 2 hours at 550 °C with a heating ramp of 10 $°C▪min^{-1}$. After the activation method, a mixed flow stream prepared with 10 $cm^3▪min^{-1}$ of CO, 30 $cm^3▪min^{-1}$ of steam (deionized water ex-situ vaporized and introduced to the reactor at 150 °C), and 60 $cm^3▪min^{-1}$ of N_2 was sent to the reactor. The catalyst (30 mg) was mixed with 2 cm^3 of SiC of 60 mesh to promote the heat and flow homogeneous distribution along the bed. The thermocouple was positioned carefully inside the catalyst bed to control the reaction temperature. The activity tests were conducted from 160 °C to 360 °C with a Δ=20 °C. The effluent was then sent to an Agilent GC 4020B gas chromatograph with Molsieve 13x, 45/60 and HayeSepQ, 80/100 packed columns. Eight injections were done at each temperature every 18 minutes. Additionally, Tedlar bags were filled in a valve set before the condenser to analyze the full content of the effluent in an Agilent GC 8120 multidimensional gas chromatograph (MDGC) equipped with a modulator, an HP-Innowax 5mx0.25 mm, and a DB-5MS 30mx0.25 mm packed columns to verify whether the presence of other light components was formed or not. The reaction set is presented in Scheme 1. The catalytic activity was expressed in terms of the CO conversion; the mass balance was corroborated with MDGC.

2.3.2. In situ activity measurements

The FTIR characterization under reaction conditions was performed in an Agilent 660 spectrophotometer, using an ISRI transmission heated-cell and in-situ high-low pressure infrared reactor with ZnSe windows. Self-supporting wafers of the catalysts with a thickness of 24 $mg.cm^{-2}$ were prepared by pressing the powdered samples at a pressure of 10×10^3 $kg▪cm^{-2}$ for 10 min. Prior to experiments, the self-supporting wafers were treated with 40 $cm^3▪min^{-1}$ of H_2 at 550 °C for 1 h to reduce the catalyst. Then, the sample was cooled down to 160 °C. After the thermal treatment stage, the flowing gas was switched to 50 $cm^3▪min^{-1}$ of the mixture CO/N_2 (4.2% v/v CO, balance N_2), which was saturated with water at 20 °C The temperature of the FTIR reactor/cell was increased to 360 °C. The infrared spectra were recorded with a resolution of 4 cm^{-1} for every 20 °C temperature increase. Tedlar bags were filled to analyze the full content of the in-situ cell effluent in the Agilent GC 4020B gas chromatograph.

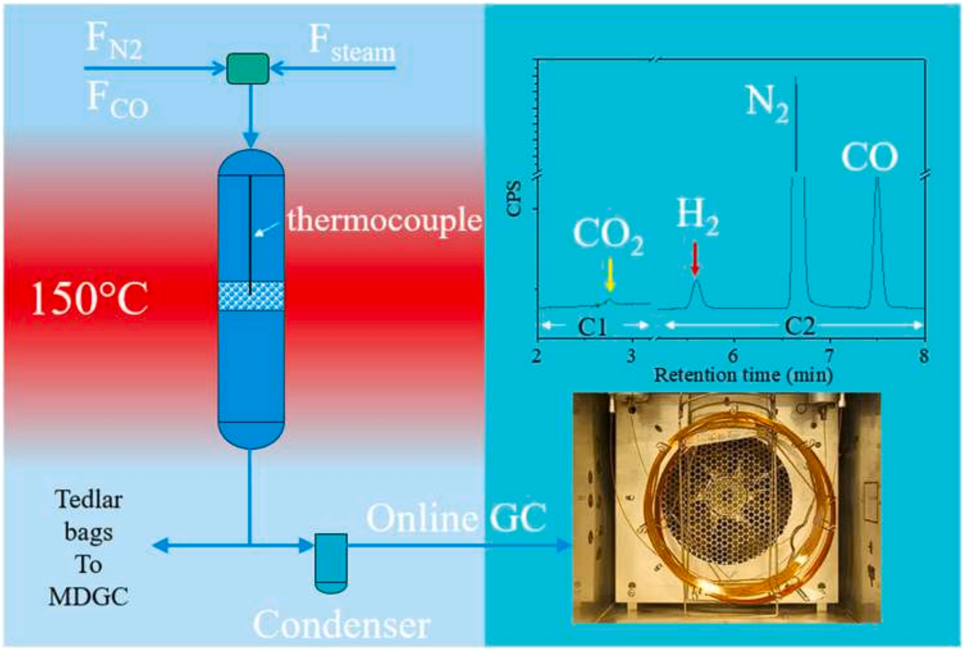

Scheme 1. Catalytic activity test system with an online GC.

2.4. Characterization techniques

Morphology and chemical mapping were obtained in a scanning electron microscope (JEOL JIB-4500). STEM micrographs were collected on a JEOL-2010 F. Samples were suspended in n-heptane and deposited on Lacey carbon (440 Mesh) on Cu grid holders. For the identification of crystalline phases, AERIS equipment (Malvern Panalytical) with Cu radiation = 0.15406 nm) was used. The measurement parameters were a scanning speed of 0.02° every 0.5 s in a range of Bragg angles (2θ) between 10° and 80°. A TriStar II 3020 (Micrometrics) was used to determine textural properties such as specific area, pore volume, and pore size distribution. Prior to N_2 physisorption, the samples were subjected to a vacuum degassing treatment at 300 °C for 8 h to remove gaseous contaminants and/or liquids retained in the pores of the supports and catalysts. They were then subjected to increasing N_2 pressures until saturation was reached. From the data taken at relative pressures below P/P0 = 0.3, the specific surface area was obtained by applying the Brunauer, Emmett, and Teller equation (BET method). The Barrett-Joyner-Halenda (BJH) method was used to calculate pore size. The calculation of the zero point of charge (ZPC) of the supports was performed using the Zetasizer Nano ZS dynamic light scattering equipment (Malvern Panalytical). 200 mg of material was dispersed in 20 mL of 0.01 M NaCl. Titration was performed using 0.01 M HCl and 0.01 M NaOH solutions. The ZPC of the materials is determined at the intersection with the abscissa of the curve obtained with the points of potential Z vs pH. The XPS spectra of the samples were recorded using a SPECS® spectrometer with a PHOIBOS® 150 WAL hemispherical energy analyzer with angular resolution (< 0.5 degrees), equipped with an XR 50 X-Ray Al-X-ray and μ-FOCUS 500 X-ray monochromator (Al excitation line) sources. The binding energies (BE) were referenced to the C 1 s peak (284.8 eV) to compensate for the charging effects. The analysis was performed on the samples after their activation using the procedure described in Section 2.3.1. The glass U-shaped reactor used for the activation was sealed with quick connection valves and kept under the N_2 atmosphere before their analysis. Then, the reduced samples are transferred to the N_2 glove box chamber to be placed in the XPS holder equipped with indium foil. The holder with four samples is transferred to the XPS mobile chamber, which is connected to the N_2 glove box via a KF connector. Then the XPS mobile chamber's gate valve is closed, and N_2 is evacuated. Afterward, the mobile chamber is connected to the XPS equipment via the KF port. The BE and intensities for the chemical quantification are determined after subtracting a Shirley-type background from the photoemission spectra using Casa XPS software (ver. 2.3.24). The composition is calculated from the experimental areas and corrected using Scofield's photoionization sensitivity factors. A deconvolution process with Gaussian–Lorentzian curves was used to analyze each spectrum.

2.5. Theoretical calculations

To determine the role of the Ga and Y incorporation into the Al_2O_3, a series of first-principles calculations were carried -using the Density Functional Theory framework- as implemented in the Vienna Ab Initio Simulation Package [29–31]. Al, O, Ga, Y, and Ni atoms were treated with projector-augmented wave pseudopotentials [32,33]. The electronic states expanded as plane waves were optimized to a cutoff energy of 500 eV. The level of theory utilized to approximate the exchange and correlation energies was the generalized gradient approximation in the simple and transferable parametrization proposed by Perdew, Burke, and Emzerhof [34]. Every treated system was considered converged in energy and force once they fulfilled the following criteria: 1 meV and 0.01 eV/Å, respectively. Integrations in the Brillouin zone were carried out using an equally distributed mesh of k-points under the approximation made in [35]. A 4×4x4 k-point mesh was optimized to treat the Al_2O_3 bulk structure. After that, the most stable clean/dry (0001) surface structure was modeled following the full method described in [36].

2.5.1. Model system and stability assessment

To understand the Ga, Y, and Ni interaction with the Al_2O_3(0001) surface. First, we modeled a 1×2 surface periodicity slab comprising 13 at. layers (7 Al and 6 O layers) that meet the Al_2O_3 stoichiometry. Structural relaxations were carried out without any constraints using a 5×5x1 k-point mesh. After complete optimization, the first Al relaxed towards the second O layer, reaching almost the same perpendicular distance. Similar results were observed by Chen et al. [36]. After that, we adsorbed and incorporated Ga, Y, and Ni atoms on the (0001) surface and subsurface of Al_2O_3. We considered surface adsorption and a scenario in which the foreign species replaced host Al atoms in the first, second, and third monolayers. Since we are considering Al deficit because Ga, Y, and Ni may be taking on their surface sites, the total energies are no longer a good parameter for determining their stabilities. Instead, the surface formation energy formalism is more appropriate since it does not depend on the number of atoms but on the chemical potentials of the involved species. Here, we treat it in its most general form,

$$E_f = E_{slab} - E_{ref} - \sum_i n_i \mu_i$$

where E_{slab} stands for the total energy of each treated system; these may include Ga, Y, Ni, and the co-incorporated Ga-Ni and Y-Ni atoms. E_{ref} represents the energy of the reference system. In this case, the clean/dry structure. n_i and μ_i define the deficit or extra ith species. For example, if E_{slab} has an Al atom less than E_{ref}, n_i must take the -1 value. In the case of Ga, Y, and Ni atoms, n_i must be positive, meaning an excess of the previously mentioned atoms. μ_i represents the chemical potential of all the involved species. It is obtained in a solid state and at zero temperature as the total energy of their most stable bulk structure. In the case of the gas phase molecules like O_2, the chemical potential was calculated as an isolated molecule into a supercell with a=20 Å. To evaluate the formation energies, we need to consider different growth conditions, and these are defined by the Al_2O_3 formation enthalpy, which is equal to −3.03 eV/atom and is in close agreement with the experimental value reported in [36] and the references therein.

3. Results

3.1. Supports

3.1.1. Scanning electron microscopy

Fig. 1 shows the SEM micrographs obtained from the pure Al-0 (Al_2O_3), AlGa-100 (Ga_2O_3), and AlY-100 (Y_2O_3) samples prepared by the hydrothermal synthesis described in Section 2.1. As can be seen in Fig. 1A, related to the Al-0 sample, there are multiple urchin-like hollow microspheres formed by nanorods and nanoneedles of different sizes. We previously reported obtaining this type of morphology in materials used as catalysts for the dehydration of secondary alcohols. Mendoza-Nuñez et al. mentioned that the urchin-like nanoparticles resulted with diameters of around 2.4 ± 0.6 µm, the 2D nanobelts had a length of 1.3 µm and a wide of 97 nm, while the 1D nanorods resulted with similar length as nanobelts but with diameters of 14 nm [37]. In Fig. 1B, the AlGa-100 reference material prepared using the same hydrothermal synthesis conditions showed structures in the form of octahedral parallelograms of different sizes. The parallelograms presented average lengths of 8.4 ± 0.2 µm for the long faces, while the rhombohedral faces in the base presented average widths of 1.3 ± 0.1 µm. On the other hand, the AlY-100 material presented in Fig. 1C showed non-uniform agglomerates and apparently some rounded microparticles that resemble spheres. Nevertheless, due to the unclear morphology, we were not capable of obtaining a statistical analysis of this case.

In the case of the AlGa-x and AlY-x mixed oxides, their morphology presented clear differences as a function of the Ga_2O_3 or Y_2O_3 content with respect to the pure oxide shapes. The SEM micrographs obtained from the mixed oxide samples are provided in Fig. 2. The AlGa-25 (Fig. 2A) presented large rod arrays and microspheres of different sizes not homogeneously distributed. Clearly, the hollow spheres urchin-like morphologies observed in the Al_2O_3 sample disappeared from the general view. In the AlGa-50, the quantity of microspheres decreases considerably. Instead, the fiber-like agglomerates begin to grow, giving place to large rectangular-shaped particles, as reported in [38].

On the other hand, for the AlY-25, we observed similar general morphology to that of the AlGa-25, although the spheres and rod arrays seem to be smaller. A rapid statistical analysis showed that the spheres in the AlGa-25 were 22% larger than those in the AlY-25. In the case of the nanorods, both materials presented similar diameters. However, in the AlY-50, the nanorod arrays almost disappeared, and the microspheres seem to be homogeneously sized. The nanorods disappeared with the increase in the Y_2O_3 contents reported previously in [26].

The morphology of the samples Ni/Al-0, Ni/AlGa-x, and Ni/AlY-x catalysts presented the exact morphology as their supports, indicating good dispersion of Ni over the samples until the detection limit of this technique.

3.1.2. X-ray diffraction

The diffractograms obtained from the Al-0, AlGa-x and AlY-x systems are provided in Fig. 3. The AlGa-x system is provided in Fig. 3A. It is possible to observe in the diffractograms of the Al-0, AlGa-25, and AlGa-50 three broad peaks at around 36.7, 45.7 and 66.7 2θ degrees. The JCPDS-01–077–0403 crystallographic data sheet indicated that those peak positions correspond well with (111), (100), and (110) planes of γ-Al_2O_3 phase, respectively. In contrast, the AlGa-100 sample presented high intensity peaks at 24.5, 33.6, 35.9, 50.2, 54.9, 50.0, 63.2, and 64.6 2θ degrees. Those peaks belong to α-Ga_2O_3 with a trigonal-rhombohedral crystalline system and R-3c space group, as indicated in the JCPDS-01–085–0988 crystallographic data sheet. The peaks related to the formation of cubic $GaAl_2O_4$ sub-superficial spinel were not observed [28]. For the Al-0 sample, the cell parameter resulted in 7.901 Å, which is close to 7.906 Å reported in the crystallographic data sheet mentioned before (vide supra). In the AlGa-25 and AlGa-50, the calculated values for the cell parameter resulted in 0.511 Å and 0.512 Å, respectively, indicating a contraction in the cubic cell. Besides, the crystal size for Al-0 resulted in 8.0 nm, while for the AlGa-25 and AlGa-50, the value resulted in 10.2 nm and 9.4 nm, respectively.

Fig. 3B presents the diffractograms of the AlY-x system. In this case, the AlY-100 showed peaks at 29.2, 33.8, 48.6 and 57.6 2θ degrees. Those mentioned peaks refer to the planes (222), (400), (440), and (622) related to the cubic system of the yttrium oxide with Ia3 space group as indicated by the JCPDS-00–001–0831 data sheet. For the AlY-25 mixed

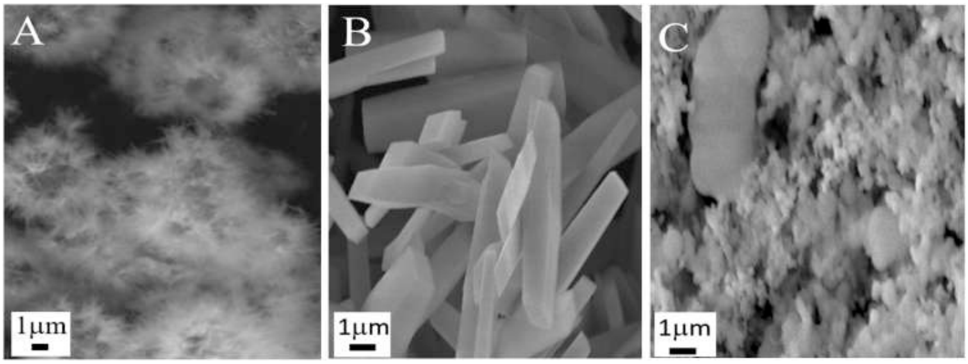

Fig. 1. SEM micrographs for the A) Al-0, B) AlGa-100 (Ga_2O_3) and C) AlY-100 (Y_2O_3) pure oxides samples calcined at 500°C.

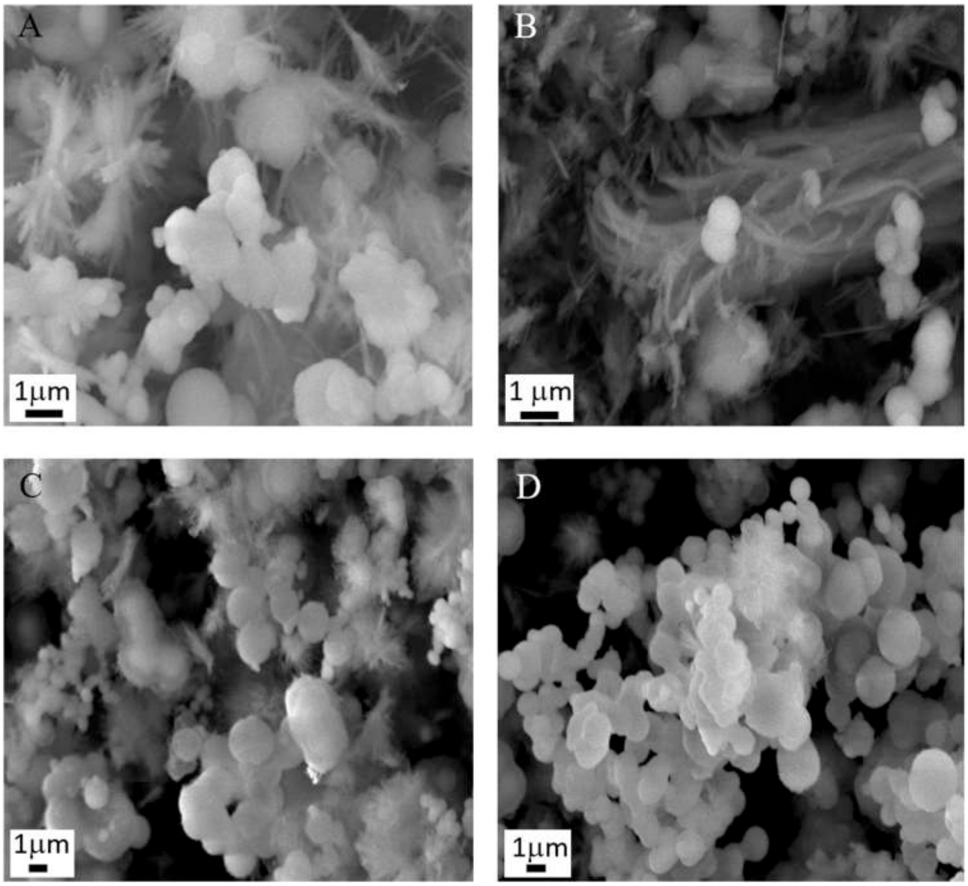

Fig. 2. SEM micrographs obtained from the A) AlGa-25, B) AlGa-50, C) AlY-25, and AlY-50 samples.

oxide, only the most intense peaks of the alumina phase were observed, although their decreased intensity indicated a loss in its short-range crystallinity. The AlY-50, by contrast, presented the peaks at 29.2 and 33.8 2θ degrees of the yttrium oxide. Additionally, this sample exhibited two peaks at 30.6 and 31.7 2θ degrees that could be related to the hexagonal $YAlO_3$, according to the crystallographic data sheet JCPDS-01–074–1334. The cell parameter for the cubic system of AlY-25 and AlY-50 resulted in 10.30 Å and 10.31 Å, respectively. Additionally, the particle size of these materials resulted in 13.3 nm and 14.8 nm for the AlY-25 and AlY-50, respectively [26].

3.1.3. Textural properties

The textural properties of the Al-0, AlGa-x and AlY-x samples are presented in Table 1. The specific surface areas (S_{BET}) of the Al-0 sample resulted in 223 m^2■$g^{-1,}$ which is in good agreement with the value previously reported for this sample [26,27]. For the AlGa-x and AlY-x series, we found a systematic decrease in the textural properties with the increase in gallium oxide or yttrium oxide in the samples. For example, the decrease in the textural properties for the AlY-25 was only 17% with respect to the Al-0 sample. Meanwhile, in the case of AlGa-25, the decrease resulted in around 30%. As expected, the pure oxides AlGa-100 and AlY-100 resulted in 24 m^2■g^{-1} and 20 m^2■g^{-1} being the lowest value of specific surface area obtained among the samples. These AlGa-100 and AlY-100 pure oxide samples will not be further used for the preparation of catalysts due to the low impregnating surface area available, which will cause poor Ni dispersion. In the case of the pore volume (P_V) the alumina sample presented the highest value of 0.35 cm^3■g^{-1} followed by the AlY-25 sample with 0.25 cm^3■g^{-1}. These low pore volume values observed in Table 1 reflect that the particles observed are rather solid than porous materials. The porosity found by this technique is probably more related to the voids generated by the interconnection of the nanostructures than to real pores, as it has been reported for similar materials.

3.1.4. Point of zero charge

The values of PZC are listed in Table 1. As observed, the values increase slightly with the presence of Ga_2O_3 in the samples. Nevertheless, the values increase to 9.15 and 9.18 for AlY-25 and AlY-50, respectively. These results imply that AlY-x samples will interact strongly with the Ni species during the impregnation procedure since typically, the Ni precursors generate acid-aqueous solutions. Also, this higher basicity observed on the AlY-x samples could induce larger or at least better interaction with CO.

3.2. Catalytic activity measurements

The catalyst activity measurements require the catalysts to be in a reduced state. The literature reported that the reduction of Ni begins around 400 °C with the maximum around 490 °C to 530 °C, with the end of the Ni reduction around 540 °C depending on the support [39]. Our results of TPR confirmed the results described before for the Ni/Al-0 as seen in the TPR provided as supporting information in Figure S1. Therefore, all the samples were reduced at 550 °C to ensure the Ni catalysts were successfully activated regardless of the support.

3.2.1. Continuous flow microreactor

The evaluations were conducted under a differential regime using a gas hourly space velocity (GHSV) of 30,000 h^{-1}; therefore, conversions obtained were below 10% even in the higher temperature analyzed. Also, it is worth mentioning that the first temperature analyzed was the highest (360 °C), as Carberry suggested for laboratory catalysts evaluation [40]. The average conversion in each temperature was obtained

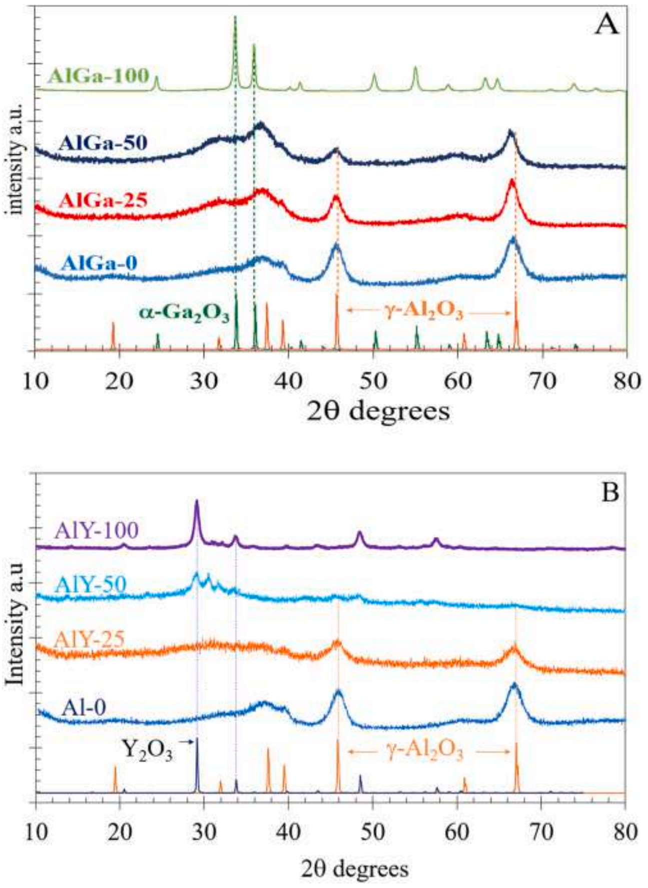

Fig. 3. A) XRD diffractograms of the AlGa-x and B) AlY-x systems.

Table 1
Textural properties and PZC of the calcined samples AlGa-x and AlY-x. Surface area (S_A), pore volume ($\boldsymbol{P_v}$) and average pore size ($\boldsymbol{P_s}$).

	S_{BET} m^2■g^{-1}	Pv cm^3■g^{-1}	Ps nm	PZC pH
Al-0	223	0.35	6.1	8.03
AlGa-25	156	0.2	4.8	8.11
AlGa-50	120	0.1	4.2	8.10
AlGa-100	24	0.03	6.8	8.11
AlY-25	190	0.25	5.7	9.15
AlY-50	142	0.18	7.4	9.18
AlY-100	20	0.06	6.1	8.35

under steady-state conditions. The Ni/Al-0 sample presented around 6% conversion at 360 °C during stabilization (see Fig. S2). The sample was cooled down to 160 °C and stabilized at this temperature during 3–8 samples; then, the temperature was increased again to 180 °C. The same procedure was done until the temperature reached 360 °C again. The sample began to convert the CO around 240 °C and continued increasing its conversion until it reached the same values as at the beginning (360 °C). No methane was observed in the reactor effluent. This method grants that all reaction data could be used to obtain kinetics parameters as the activation energy. Fig. 4A presents the reaction rate at steady-state conditions, and Fig. 4B displays the Arrhenius plot from where we obtained the activation energy for all the samples. As seen, the activity for the Ni/AlGa-x samples resulted higher among series, especially the Ni/AlGa-50 presented 45%,17%, 65%, and 45% higher activity than Ni/Al-0, Ni/AlGa-25, Ni/AlY-25, and Ni/AlY-50 respectively.

Additionally, it is possible to observe that in the case of the Ni/AlY-x series, the sample with 50% yttrium oxide coincidentally provides better activity. In the case of the apparent activation energy (E_a) all samples

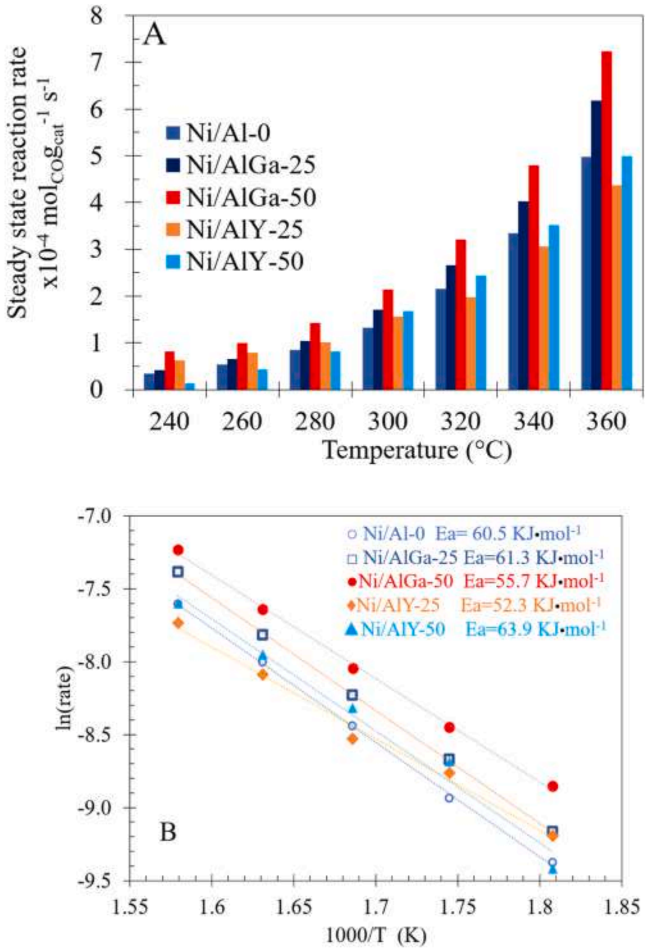

Fig. 4. A) Steady-state reaction rate and B) Arrhenius plot for the Ni/Al-0, Ni/AlGa-x and Ni/AlY-x samples.

presented values in the range of reported values for other WGS catalysts (see Fig. 4B) [7,41,42]. From those, the lower values of E_a were observed in the Ni/AlY-25 with 52.3 KJ■mol^{-1}. CO% conversion plots related to the Ni/AlGa-x and Ni/AlY-x catalysts are provided in the supplementary information as Fig. S3.

3.2.2. In-situ FTIR measurements

To understand how the incorporation of yttrium and gallium oxides into the support induces changes in the catalytic activity of Ni catalysts, we decided to evaluate the Ni/Al-0, Ni/AlGa-25, and Ni/AlY-25 samples since they displayed different activity behavior in all range of temperatures evaluated under steady-state conditions. The samples were in situ characterized by infrared spectroscopy to determine the surface species involved in the catalysis. These experiments were conducted under reaction conditions similar to those of the catalytic activity tests in Section 3.2.2. Simultaneously, the composition of H_2 and CO_2 in the outlet gases was analyzed by GC. Fig. 5 presents the in-situ FTIR measurements for all samples.

In the first place, the Ni/Al-0 sample was set into the reaction cell and activated as described in Section 2.3.2. The inflow of the reactive mixture into the FTIR Cell at 160 °C generated several bands in the IR spectrum of the Ni/Al-0 sample, as observed in Fig. 5A. The doublet bands at 2177 cm^{-1} and 2111 cm^{-1} can be assigned to carbon monoxide in the gas phase [43,44]. The bands at 1586 cm^{-1} and 1394 cm^{-1} can be assigned to the $\upsilon_{a(CO2)}$ and $\delta_{(CH)}$ vibration modes of surface formate species bonded on γ-Al_2O_3 in bidentate configuration, respectively [45] Some authors have proposed that these species can be originated by the interaction between CO_{gas} and surface hydroxyl groups at temperatures

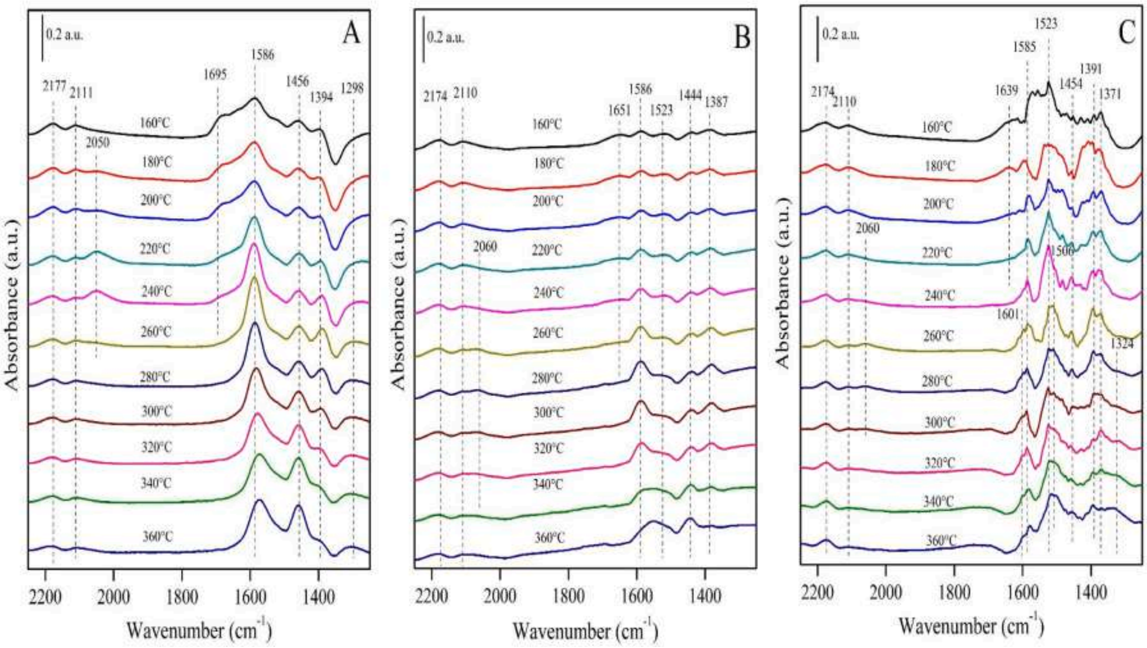

Fig. 5. FTIR characterization of the A) Ni/Al-0 sample, B) Ni/AlGa-25, and C) Ni/AlY-25 samples under reaction conditions.

higher than 100 °C [46]. The band at 1695 cm^{-1} can be assigned to asymmetric stretching of bridged carbonate species (br-carbonate) on the support (γ-Al_2O_3)[47]. The bands at 1456 cm^{-1} and 1298 cm^{-1} can be due to the $\upsilon_{a(CO3)}$ of ionic carbonate (i-carbonate) and $\upsilon_{s(CO3)}$ of carbonate in bidentate form (b-carbonate) on alumina [47]. Carbonate species on the surface could be due to the adsorption of CO_2 or the oxidation of formate species. Given that, at this temperature (160 °C), carbon dioxide was not detected in the outlet gases (Fig. 6A), it is assumed that a part of the formate species is responsible for the carbonate species formation. Evidence of nickel carbonyls was not seen at this temperature, demonstrating that carbon monoxide is adsorbed on the surface of the support, mainly on hydroxyl groups, which can be generated by the dissociative adsorption of water on Al_2O_3 (Al^{+3}-OH and O^{-2}-H)[48].

With the temperature increase, changes in the IR spectra were observed (Fig. 5A). The bands of formate species (1586 and 1394 cm^{-1}) increased their intensities until they reached their maximum value between 240 °C and 260 °C. Simultaneously, a new band at 2050 cm^{-1} emerged at 180 °C, which can be attributed to C-O bond stretching ($\upsilon_{(CO)}$) of carbonyl species bonded on Ni^0 linearly [49]. Its maximum intensity was reached at approximately 240 °C. Its origin could be due to the dehydroxylation process of formate species (HCO_2^-) on Al_2O_3 around Ni^0 sites [50]. Also, the band attributable to br-carbonate decreased until it disappeared at approximately 240 °C. This species disappeared probably because of the thermal desorption effect caused by the temperature increase. Above 240 °C, the characteristic bands of formate species, both related to CO gas, decreased gradually; in parallel, the concentration of CO_2 and H_2 in the outlet gases increased continuously with temperature (Fig. 6A). As both phenomena happen simultaneously, formate species are assumed to be converted to CO_2 during the catalysis transformation step. Some authors have proposed that due to formate species decomposition, CO_2 gas and H adatoms can be formed, which

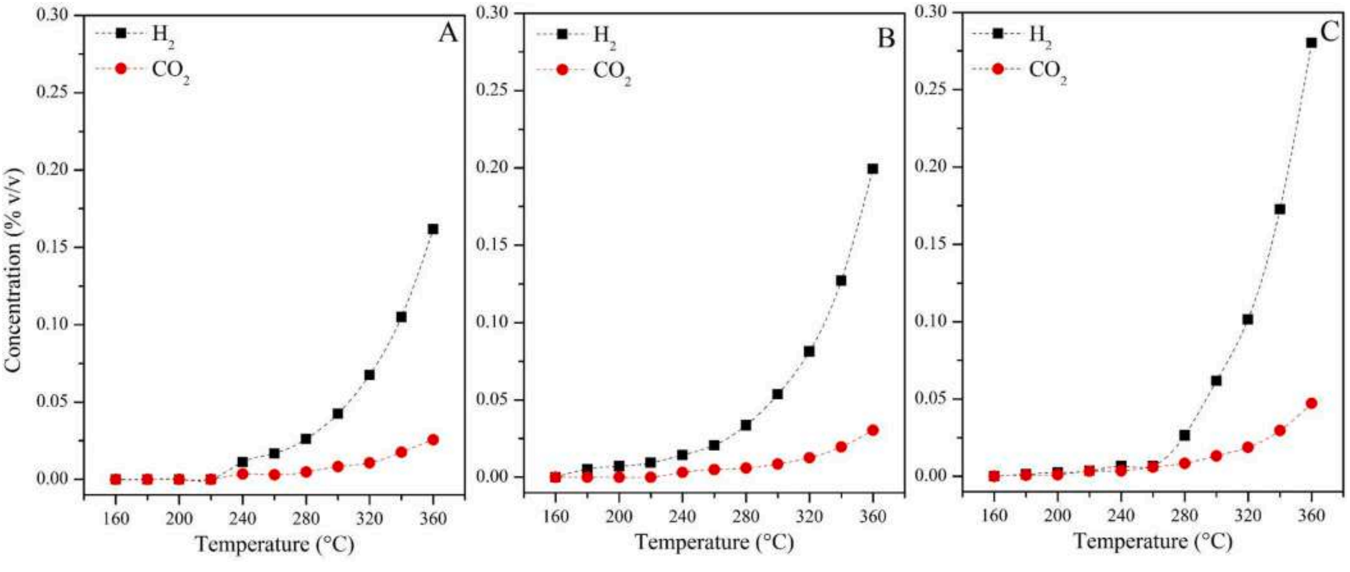

Fig. 6. Concentration (in %v/v) of CO_2 and H_2 in the outlet gases of the FTIR reactor/cell for Ni/Al-0, Ni/AlGa-25, and Ni/AlY-25 samples under reaction conditions.

can be combined to form H_2 on the surface of Ni nanoparticles [51].

In the experiment, the bands of ionic (1456 cm^{-1}) carbonate increased with the increase in temperature. Meanwhile, the band assigned to the bidentate carbonate (1298 cm^{-1}) remained constant or barely decreased in intensity as a function of temperature. This behavior suggests that both species act as spectators and do not participate in the catalysis process. By contrast, the presence of these species over the surface indicates the use of active sites to be adsorbed, which considerably decreases the activity. For its part, the decrease in the intensity of the band of nickel carbonyls can be associated with the thermal desorption of CO_{gas}.

In the case of an in-situ reaction experiment using the Ni/AlGa-25 sample (see Fig. 5B), when CO_{gas} and steam were put in contact with the sample, the same vibrational modes were observed, although the position of the bands appeared slightly shifted in comparison to that observed for the Ni/Al-0 sample. Nevertheless, the intensity of these bands was lower in the spectrum of the Ga-containing material than in the Ni/Al-0 sample (Fig. 5A). This is related to the gallium incorporation modifying the surface acid/base properties in comparison to the Al-0 support as indicated by the ZPC values presented before. The band at 1651 cm^{-1} can be assigned to the $\upsilon_{a(CO3)}$ vibration mode of bicarbonate species on Al_2O_3/Ga_2O_3 [47,52,53]. At the same time, the bands at 1523 and 1444 cm^{-1} can be due to the $\upsilon_{a(CO3)}$ vibration mode of monodentate and ionic carbonate [47,52]. Again, the origin of carbonaceous species could be the oxidation of a portion of formate species, as in the Ni/Al-0 sample case. When the temperature increased, the bands of formate species also increased, reaching their maximum intensity at 260 °C (Fig. 5B). Above this temperature, these bands began to decrease progressively. Concomitantly, the production of CO_2 and H_2 also increased, as was evidenced by the concentration in the outlet gases (Fig. 6B). At the same time, the bands of CO gas decreased (Fig. 5B). Both events confirm the assumption that formate species participate actively in the production of CO_2 along with one H atom on the surface of the active metal, whose reaction with another H atom (promoted on the Ni surface) form H_2.

As compared to what was observed for the Ni/Al-0 sample, the nickel carbonyl band, possibly due to the dehydroxylation of formate species on the metal-support interface, was less intense, especially at lower temperatures[50]. Also, the bands of carbonate species remain constant even at 360 °C. Based on this observation, it is determined that they do not participate in the catalysis; contrarily, they can block the active sites. However, unlike Ni/Al-0, the intensity of this band was lower, which can explain the increment in the catalytic activity of the Ga-containing samples.

On the other hand, the spectra of the Ni/AlY-25 obtained under reaction conditions are shown in Fig. 5C. The admission of the reactive mixture into the FTIR cell originated the appearance of several bands in the IR spectrum at 160 °C. Formate species were also observed likewise as in the other two samples, which was evidenced by the presence of the bands at 1585 ($\upsilon_{a(CO2)}$), 1391($\delta_{(CH)}$), and 1371 cm^{-1} ($\upsilon_{s(CO2)}$). Again, their origin could be due to the reaction of CO gas with hydroxyl groups generated by the dissociative adsorption of water vapor [48]. Also, carbonaceous species were detected in the IR spectrum according to the bands at 1639, 1523, and 1454 cm^{-1} assigned to $\upsilon_{a(CO3)}$ vibration mode of bicarbonate species and monodentate and ionic carbonate, respectively [47,52]. Whose formation can be explained by the oxidation of formate species. The additional two bands at 2174 and 2110 cm^{-1} are assigned to carbon monoxide in the gas phase.

With the temperature increase, the band of bicarbonate species (1639 cm^{-1}) decreased until it disappeared at 220 °C (Fig. 5C). As CO_2 was not detected in the range between 160 and 220 °C in the outlet gases (Fig. 6C), it is inferred that the bicarbonates are not desorbed; instead, they are transformed into another surface species. The heating of the sample under the flow of the reactive mixture generated an increment in the intensity of the bands of formate species (1585 ($\upsilon_{a(CO2)}$), 1391($\delta_{(CH)}$), and 1371 cm^{-1} ($\upsilon_{s(CO2)}$) until they reached the maximum intensity at 260 °C (Fig. 5C). Above this temperature, the value of these bands began to decrease. At the same time, the concentration of CO_2 and H_2 in the outlet gases increased gradually (Fig. 6C). Both observations suggest that formate species participate in the catalysis of the water gas shift reaction, which was bolstered by the decrease of the CO gas bands above 260 °C (Fig. 5C).

During the experiment, nickel carbonyls were observed from 220 °C to 300 °C in the IR spectra (Fig. 5C). Above 260 °C, two new bands emerged at 1601 and 1324 cm^{-1} attributable to the $\upsilon_{a(CO3)}$ and $\upsilon_{s(CO3)}$ of bridged carbonate species bonded to Y_2O_3 (possibly originated by the oxidation of formate species)[54]. The intensity of these signals reached a maximum between 300 and 320 °C, then decreased. It is probable that they are desorbed as O-CO. This additional route at high temperatures could explain the increment in the CO_2 (and H_2) production on this sample compared to the Ni/Al-0 catalyst.

3.3. *Catalysts characterization*

3.3.1. *XPS*

The surface analysis of the Ni catalysts supported on the AlGa-x and AlY-x samples displayed the presence of typical photopeaks related to Ni, Al, Ga, Y, O and C atoms. The surveys showed the core emission line regions for those atoms depending on their composition. Fig. 7 presents the high-resolution spectra for the Ga 2p (A) and Y 3p (B) core emission line regions for the AlGa-x and AlY-x samples. It is possible to observe that Ni/AlGa-25 (Fig. 7A-a) and Ni/AlGa-50 (Fig. 7A-b) samples were characterized by the Ga 2p photoelectron spectrum with the Ga $2p_{3/2}$ and Ga $2p_{1/2}$ spin-orbit splitting components. The Ga $2p_{3/2}$ was observed at 1117.6 eV with a shift (Δ) of 26.9 eV for the Ga $2p_{1/2}$. In the case of the AlY-25 (Fig. 7A-c) and AlY-50 (Fig. 7A-d) presented in Fig. 7B, the Y 3d photoelectron region appeared as a single broad peak centered at 157.6 eV. The two spin-orbit splitting components Y $3d_{3/2}$ and Y $3d_{1/2}$ were not discernable due to the small spin-orbit splitting Δ of 2.05 eV. As expected, the observed photoelectron peaks increase in intensity in both regions as the gallium oxide or yttrium oxide contents increase.

The semiquantitative chemical analysis is presented in Table 2. In the Ni/Al-0 sample, the weight % (wt%) for the Al and O atoms resulted around the expected nominal values, although the presence of 7.4 wt% of carbon could explain their slightly lower values. In the case of Ni, the 5.0 wt% expected value was not obtained, indicating that 60% of impregnated Ni enters into the sub-superficial layers by migration and possibly forming $NiAl_2O_4$ spinels as reported by Topsoe et al. [55]. In the case of samples Ni/AlGa-25 and Ni/AlGa-50 the Ni content resulted in 3.3 wt% and 4.7 wt%, respectively. These results suggested that the Ni increases on the surface as the Ga_2O_3 increases in the support. For the samples Ni/AlY-25 and Ni/AlY-50 the Ni content resulted in 5.6 wt% and 4.8 wt%, respectively. In this case, the Ni content is around the nominal value in both Y_2O_3-containing samples, suggesting that this preparation allows the Ni to be impregnated homogeneously distributed in the support. However, a deconvolution process in the Ni 2p high-resolution window was carried out to shed light on the Ni species participating in the catalytic reaction.

Fig. 8 presents the high-resolution spectra of the Ni 2p emission region for Ni/Al-0, Ni/AlGa-x, and Ni/AlY-x samples. In the Ni/Al-0 (Fig. 8A-a), four peaks were observed at 855.8 eV, 861.8 eV, 873.6 eV, and 878.6 eV. The photopeaks at 855.8 eV and 873.6 eV are related to the spin-orbit splitting of Ni 2p with a shift of 17.8 eV. The typical shift for the spin-orbit is 17.5 eV, although this value is observed when only one unique chemical environment surrounds the Ni atom. In our case, the possibility of having more than one species is evident since the Ni/AlGa-x and Ni/AlY-x samples clearly presented an extra peak around 851.3 eV. The other broad peaks at 861.8 eV and 878.6 eV are commonly associated with shake-up satellites. It is worth noticing that the samples were ex-situ reduced prior to the analysis with the method described in Section 2.3.1. We performed a deconvolution process on

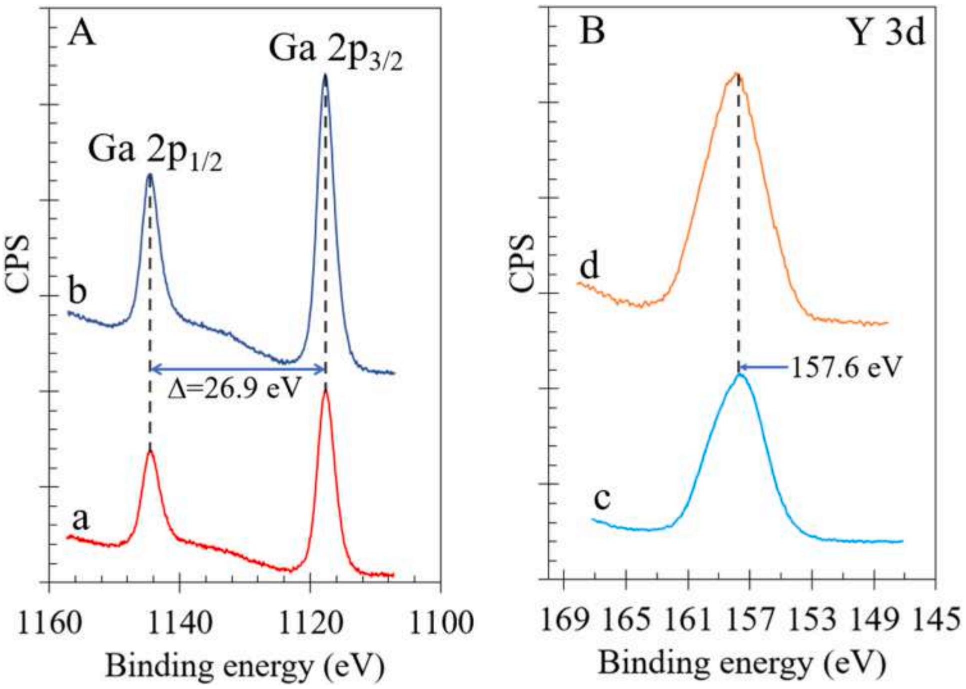

Fig. 7. XPS spectra for the Ni/AlGa-x and Ni/AlY-x samples in the high-resolution window for A) Ga 2p and B) Y 3d. a) AlGa-25, b) AlGa-50, c) AlY-25, and d) AlY-50.

Table 2
Semi-quantitative analysis of the XPS spectra for the Ni/Al-0, Ni/AlGa-x and Ni/AlY-x samples.

sample	Ni wt%	Al wt%	Ga wt%	Y wt%	C wt%	O wt%
Ni/Al-0	2.0	47.8	0.0	0.0	7.4	42.9
Ni/AlGa-25	3.3	38.5	12.6	0.0	7.9	37.8
Ni/AlGa-50	4.7	30.4	25.0	0.0	6.7	33.3
Ni/AlY-25	5.6	14.5	0.0	55.8	6.3	17.9
Ni/AlY-50	4.8	17.5	0.0	47.0	6.4	24.3

*Samples were ex-situ reduced prior to the XPS analysis

this region, considering the possible presence of Ni^0 at 852.6 eV, NiO at 855.0 eV, and $NiAl_2O_4$ at 856.7 eV [56], along with their respective satellite peak for each species (see deconvolution process for Ni/Al-0 in supplementary information as Fig. S4). Fig. 8B presents the fit in the Ni $2p_{3/2}$ emission region for the Ni/AlGa-25 (b) and Ni/AlGa-50 (c). As seen, the three photopeaks mentioned before allowed a perfect fit of the envelope, although it is clearly observed that the intensity of the species and their % differ from each other. In the Ni/AlGa-25, the photopeak assigned to the Ni^0 species resulted smaller in general terms than the NiO and $NiAl_2O_4$ photopeaks. In the Ni/AlGa-50, the Ni^0 species resulted larger, and it seems that the other two species maintain their aspect ratio. In the case of the Ni/AlY-x samples presented in Fig. 8C the behavior was precisely inverse to that in the Ni/AlGa-x system. In this case, the Ni/AlY-25 presented the larger area photopeak related to the

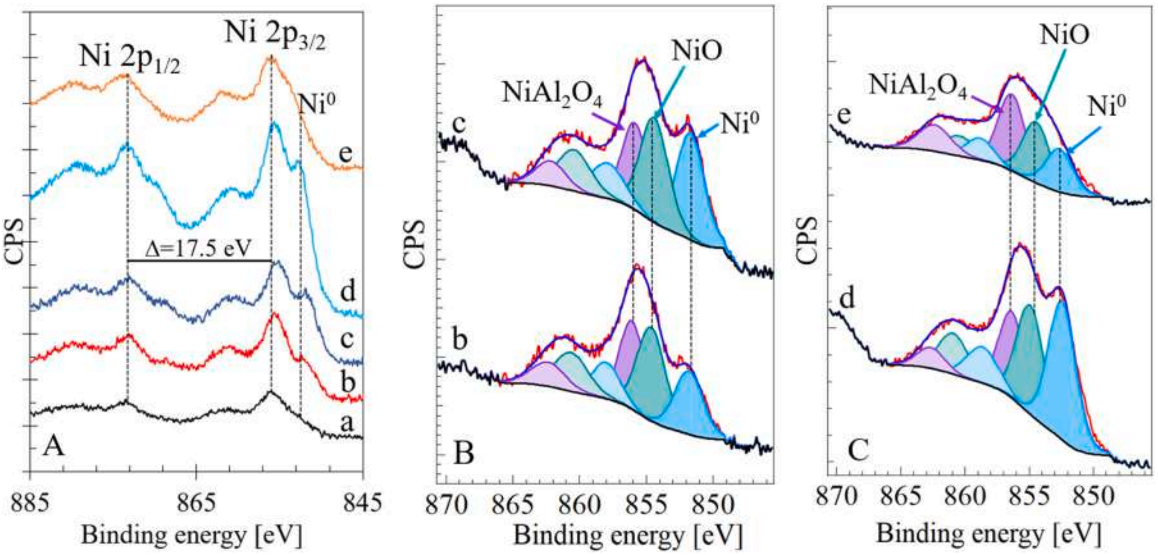

Fig. 8. A) Ni 2p XPS spectra for the a) Ni/Al-0, b) Ni/AlGa-25, c) Ni/AlGa-50, d) Ni/AlY-25, and e) Ni/AlY-50 samples, B) Ni $2p_{3/2}$ for the corresponding Ni/AlGa-x samples and C) Ni $2p_{3/2}$ for the corresponding Ni/AlY-x samples.

Ni^0 species. Furthermore, the peak related to the NiO in the Ni/AlY-50 decreased considerably with respect to the $NiAl_2O_4$ species in all samples.

The semiquantitative analysis is presented in Table 3. Ni/Al-0 sample presented around 24% of total Ni at the surface transformed into Ni^0 species. As expected, 32.5% of detectable Ni resulted in the $NiAl_2O_4$ spinel species. The remaining Ni in this sample was found to form NiO that was not reduced during the activation treatment. For the Ni/AlGa-x samples, the Ni^0 increases with the increase in the Ga_2O_3 content from 27.1% to 36.4% in the Ni/AlGa-25 and Ni/AlGa-50 samples, respectively. Meanwhile, in the Ni/AlY-x samples, the most significant quantity of Ni^0 species was observed in the Ni/AlY-25 sample, along with the lowest % of $NiAl_2O_4$ species among the series. Furthermore, the Ni/AlY-50 samples presented only 23.7% of Ni^0 species, which is a % similar to that observed in the Ni/Al-0.

3.3.2. TEM

In Fig. 9 is presented the HRTEM micrographs related to the Ni/Al-0 (A-C), Ni/AlGa-25 (D-F) and Ni/AlGa-50 (G-I) samples. The morphology of these catalysts coincides with their respective supports, in which sharp rods, along with nanobelts, form the hollow Al_2O_3 nanospheres (Fig. 9A) as presented in Section 3.1.1. Fig. 9B presents the EDX scan line analysis of a nanorod where the Al, O, and Ni atoms were detected. In this scan line, it is possible to observe that Ni atoms are present in the nanorod, but also, the belt in the background presented small peaks of Ni atoms, indicating the presence of Ni nanoparticles. The particle size analysis revealed Ni particles in a wide range, from particles below one nm to some large particles of around 10 nm. Indeed, an example of the large Ni nanoparticles detected in this catalyst is presented in Fig. 9C, in which the diameter is around 9 nm. This particle presented clearly the planes (111) of the Ni metallic phase following the interplanar distances (0.203 nm) reported in the JCPDS card 00–001–1258. In Fig. 9D the general view of the Ni/AlGa-25 is presented; this micrograph confirms the presence of nanospheres of around 20 nm of diameter induced by the gallium presence. Fig. 9E presents the Ni nanoparticles observed in this sample. Clearly, the diameter of the Ni nanoparticles resulted in the range from 3 nm to 5 nm with some particles of around 8 nm. Fig. 9F presents the micrograph of a background nanobelt with a nanorod, although, in both structures, Ni atoms were clearly observed by the EDX composition map. In Fig. 9G, related to the Ni/AlGa-50, it was observed that the structures increase in size slightly; in fact, with the increase in the gallium oxide content, the structures begin to be flat, and some large mixed oxide crystals appeared forming nanopillows as described before in [28]. These structures are presented in Fig. 9H in High Angular Annular Dark Field (HAADF) mode micrographs. Usually, the presence of large concentrations of gallium oxide in the sample made this kind of analysis difficult because it caused an intense brightness that could hide the presence of metals. Nevertheless, the bright and dark zones of both micrographs allowed us to detect the presence of Ni, which was more or less homogeneously distributed. This statement was confirmed with the EDX line scan presented in Fig. 8I, in which the intensity for aluminum and gallium resulted almost similarly to their nominal concentrations. In the case of Ni, its intensity along the scan line appears to be almost constant, indicating a homogeneous distribution. The statistical analysis of the Ni nanoparticles to obtain the average size resulted in 2.5 ±0.8 nm, 3.6 ±0.9 nm, and 4.4 ±1.1 nm for the Ni/Al-0, NiAlGa-25 and Ni/AlGa-50, respectively.

Table 3
Semiquantitative analysis on the Ni $2p_{3/2}$ high-resolution window.

Sample	Ni^0%	NiO %	$NiAl_2O_4$%
Ni/Al-0	23.9	43.6	32.5
Ni/AlGa-25	27.1	39.8	33.1
Ni/AlGa-50	36.4	36.2	27.4
Ni/AlY-25	42.2	33.1	24.7
Ni/AlY-50	23.7	33.6	42.7

In the case of the Ni/AlY-x system, Fig. 10 presents the micrographs related to the Ni/AlY-25 (A, B, C) and Ni/AlY-50 (D, E, F). In Fig. 10A, it is possible to observe the presence of a large-size nanosphere (600 nm) mainly formed by nanorods. The Fig. 10B displays a micrograph of the tip of a nanorod in HAADF mode. Clearly, the Ni nanoparticles are well dispersed over the nanostructure. The nanoparticles, in this case, resulted in around 7.8±0.3 nm as it was corroborated with the EDX line scan analysis presented in Fig. 10C. In the case Fig. 10D related to the Ni/AlY-50 the 3D microsphere resulted in around 1270 nm. Nevertheless the distribution of Ni over the surface seems to be homogeneous presenting Ni nanoparticles of sizes from 3.7 nm with an average particle size of 8.5 nm±0.6 as observed in the Fig. 10E. Using EDX line scan, it was corroborated that the 5.8 nm size nanoparticle was composed of nickel and not by yttrium, as observed in Fig. 10F.

3.3.3. Theoretical calculations adsorption and incorporation

Consider our experimental results, in which Ni and Ga are incorporated to the largest extent into the Al_2O_3 subsurface layers. At the same time, Y seems to form preferably surface species, we adsorbed and incorporated Ga, Y, and Ni on and into the Al_2O_3 (0001) clean/dry surface (see inset in Fig. 11A). Several high-symmetry sites were treated, and the ones that generated the most stable formation energies per layer are depicted in Fig. 11A. As seen, the relative formation energies (eV/Å2) for Ni on bare alumina resulted in 0.115 eV/Å2 for Ni, 0.135 eV/Å2 for Ga, and 0.18 eV/Å2 for Y, when its adsorption was simulated on the outer surface. This means these cations will migrate to the internal subsurface layers easily. The less stable values obtained among them were for those of Y. Clearly, the cation incorporation on the first layer presented similar values for the atoms tested. The results indicated that Ni could be incorporated with the same relative formation energy even on the 4th layer. Also, Fig. 11A reveals that Ga and Ni incorporate easily into the subsurface, showing similar formation energies for Ga and Ni atoms in Al sites for incorporation into the 1st, 2nd, and 4th layers. Notice that Ni and Ga are the most stable systems in the first surface layer. Turning our attention to Y adsorption and incorporation, we noticed that Y must be located mainly in the 1st surface layer. Incorporation into inner layers may be possible but with a lower probability. Also, adsorption as an adatom on the surface is even less stable. So, Y atoms will replace Al atom sites into the first surface layer only. These results confirm our experimental observation.

We further incorporated Ni atoms once the Al_2O_3 has incorporated Ga and Y atoms since our experimental evidence suggests that Ga and Y favor their surface adsorption and incorporation. We first adsorb and incorporate Ni on the Ga-modified Al_2O_3(0001) surface (Ga atoms are incorporated into the first Al layer). Results are depicted in Fig. 11B; here, we can see the Ni adsorption and incorporation into the pristine Al_2O_3 as green-color spheres. Notice that when Ga is present on the surface, Ni atoms stabilize on top of the surface and also take on Al sites into the first Al_2O_3 layer. Both structures are more stable than in the case of pristine Al_2O_3 surface and explain the experimental results in which Y increases the probability of finding surface Ni species (see red-color spheres in Fig. 11B).

4. Discussion

4.1. General

In this work, we successfully prepared Al_2O_3, Ga_2O_3, Y_2O_3, and binary mixed oxides using a hydrothermal method modified from [57]. The reference pure Al_2O_3, Ga_2O_3, and Y_2O_3 materials presented different morphology from each other. At large scale, Al_2O_3 displayed (1 μm) urchin-like hollow microspheres; these structures were clearly formed by agglomerates of nanobelts and nanorods. While the Ga_2O_3 presented rectangular bars with well-defined planes with a rhombic appearance on the base. Pure Y_2O3 showed some barely defined rounded particles, as

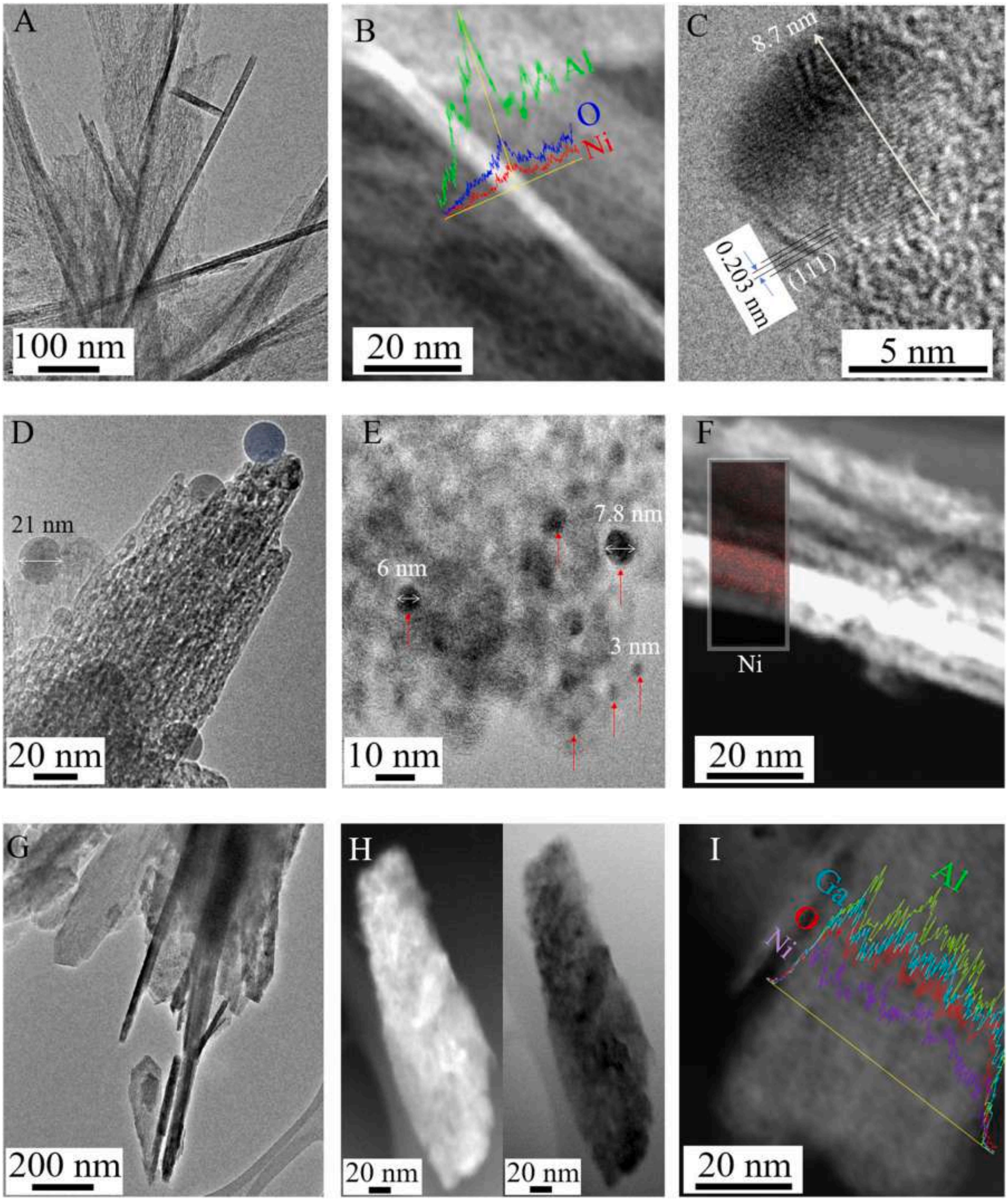

Fig. 9. HRTEM micrographs of Ni/Al-0 (A, B (EDX line scan), C), Ni/AlGa-25 (D, E, F(EDX-composition)) and Ni/AlGa-50 (G, H(HAADF), I (EDX line scan)).

seen in Fig. 1. However, the binary mixed oxides AlGa-x and AlY-x presented only nanoparticle agglomerates with sphere and rod shape. It seems that part of the urchin-like structure from Al_2O_3 remains in the low (25%) Ga_2O_3 and Y_2O_3 wt% content samples. Meanwhile, in the samples with high mixed oxide content (50 wt%) the spheres seem to predominate, especially in the AlY-50 sample. Huang et al. reported the formation of γ-AlOOH microspheres using Triton X-100 as a directing agent and urea as a precursor of ammonia, which in turn provides OH- from its hydrolysis [57] The authors mentioned that during the synthesis, Triton X-100 forms spherical micelles (51 Å) that interact with amorphous aluminum hydroxide particles to form nanospheres as large as 1 or 2 µm. Apparently, when the nanospheres base structures are formed, the next step is the growth along the perpendicular direction to the spherical surface [57]. Indeed, in previous work, some of us reported the synthesis of AlY-x samples via the hydrothermal method; we observed that the obtained nanospheres with sizes from 75 to 130 nm were formed by particles with smaller sizes, as in this case [26]. Nevertheless, one question remains unsolved: why do the mixed oxides present the solid nanosphere morphology? With the results of TEM from AlGa-25 presented in Figs. 2 and 9 and for AlY-x samples in Fig. 2 and Fig. 10, we corroborate the process described before by Huang et al., and two plausible reasons could be proposed; the first one is that the presence of Ga and Y atoms presence inhibits the perpendicular growth due to their differences on atom size compared to aluminum. The second reason to obtain these solid nanospheres could be related to improvement in particle stability, i.e. the boehmite phase forms this type of

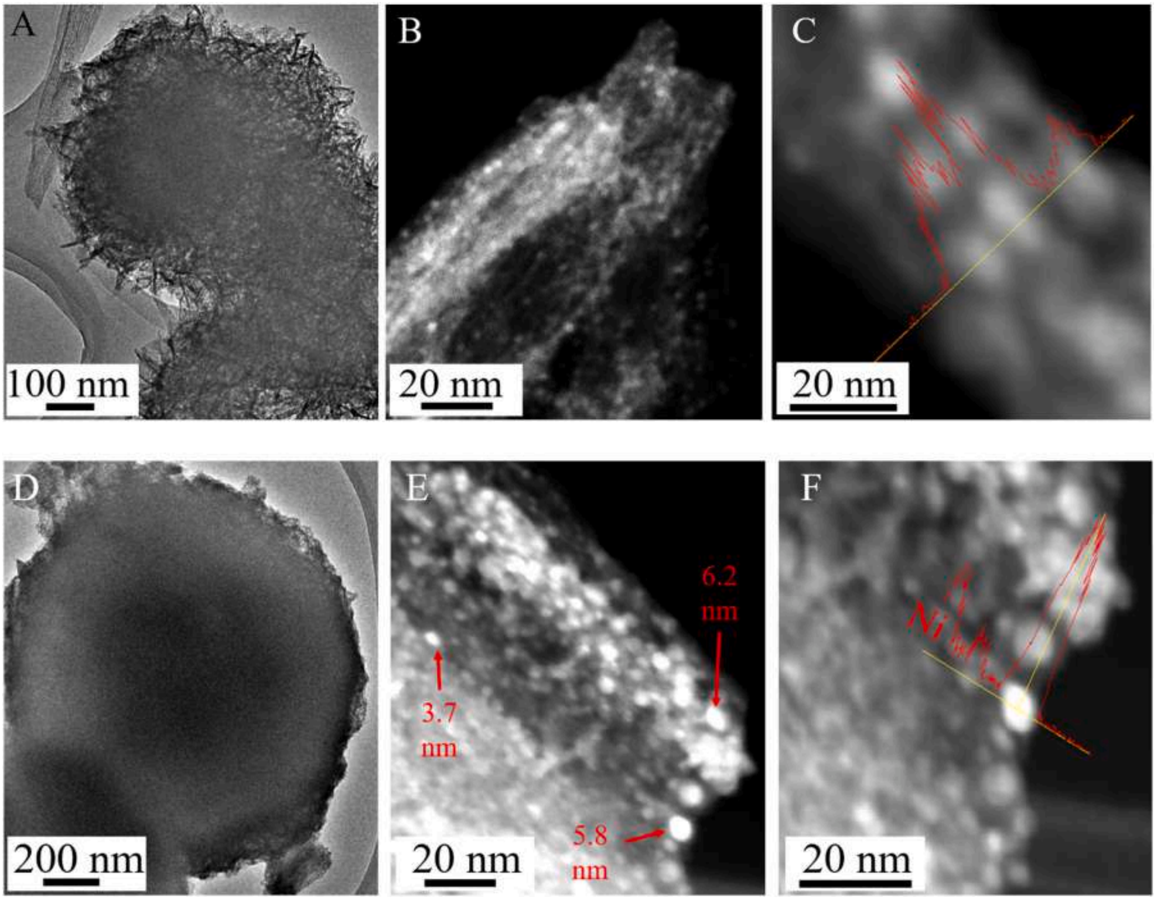

Fig. 10. HRTEM micrographs of Ni/AlY-25 (A, B, C (EDX line scan)), Ni/AlY-250 (D, E, F (EDX line scan)) samples.

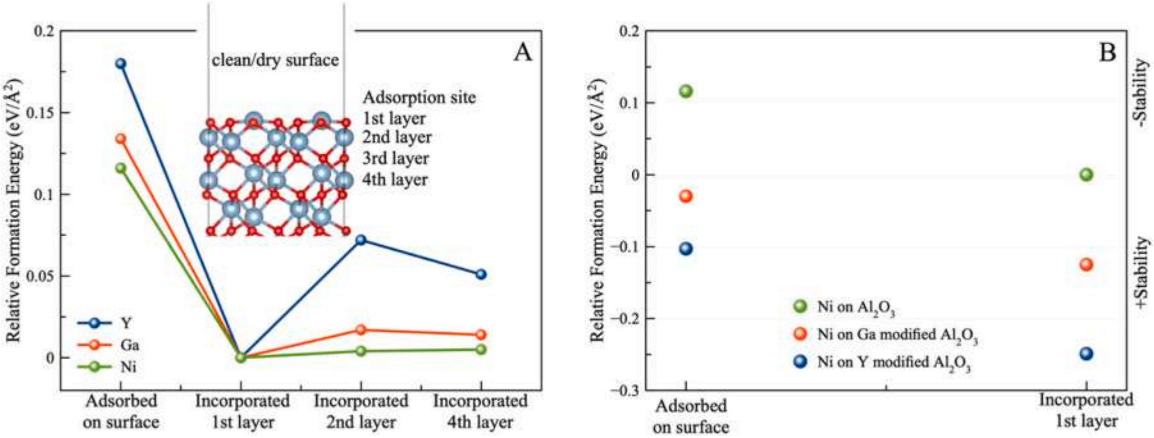

Fig. 11. A) Relative formation energies plotted as a function of the layer in which the adsorption was tested for Al_2O_3 (0001) clean surface. B) Relative formation energies plotted as a function of the layer in which the adsorption was tested for Al_2O_3 (0001) (green circles), modified with Ga atoms (orange circles) and modified with Y (navy circles).

structure during the condensation step interacting with triton X-100, but instead of continuing growing through the perpendicular direction, the system forms spherical agglomerates of several seed-nanospheres which with the thermal treatments solidify and stabilize. Although both proposals seem to be correct, several reports mentioned the thermal stabilization effect of gallium [58] and yttrium [59,60]. However, verifying the stabilization effect provided by these two atoms on our mixed oxides is out of the scope of this work. The AlGa-x samples presented similar X-ray diffraction patterns to that observed on the Al_2O_3 pure sample. In the case of the AlY-x samples, only the AlY-25 presented a similar pattern as the Al-0 sample since the AlY-50 clearly exhibited low intensity peaks related to the Y_2O_3. While the peaks of the planes (1 1 1), (1 0 0), and (1 1 0) from Al_2O_3 were not observed as seen in Fig. 3. These results suggest a good integration of gallium and aluminum to form a new binary mixed oxide with varying concentrations from 25 to 50 wt%. By counterpart, it seems that yttrium and aluminum present a certain resistance to form a mixed oxide above 25 wt% of Y_2O_3. Nevertheless, the XPS semiquantitative analysis of the samples presented in Table 2 revealed that there is more Y than Ga at the surface in the same respective wt% content samples. The calculation of the nominal ratio between Ga wt% or Y wt% and Al wt% derived in values of 0.47, 1.41, 0.5, and 1.49 for the AlGa-25, AlGa-50, AlY-25, and AlY-50 samples, respectively. Now with values reported in Table 2, the same Ga/Al and Y/Al wt% ratios conducted to the following values: 0.33, 0.82, 3.86, and 2.69 for the AlGa-25, AlGa-50, AlY-25, and AlY-50, respectively. These values confirm that Ga content is slightly lower at the surface than it has to be and is forming part of the bulk mixed oxide material. Meanwhile, the large values for the Y/Al ratio demonstrate a clear enrichment of the surface with yttrium in both AlY-25 and AlY-50 samples. This agrees with the XRD observations in which the peaks of the Y_2O_3 crystalline phase are observed. Nonetheless, the textural properties of the AlGa-x and AlY-x samples exhibited values acceptable for the intended application. However, the increase in Ga o Y in the samples considerably decreased the surface area and pore volume. However, the incorporation of Ni in the supports only resulted in an average decrease of 10% in surface area due to its low content incorporated. Our theoretical results show that when Al_2O_3 has Y incorporated into first layer Al sites, the Ni adsorption and incorporation are even more stable; see navi-color spheres in Fig. 11B. Although it would be interesting to measure the stability of Ni in inner layers, the treated systems are more stable than the pristine Al_2O_3 (0001), demonstrating that, indeed, Ga and Y induce Ni to remain as surface species. Another piece of interesting evidence appears when Y and Ga are incorporated in pristine Al_2O_3. Here, Y tends to be more stable at the surface, while Ga is stable at the surface and the subsurface layers. This means that Ga atoms could be going deeper from the surface to the inner layers, allowing Ni to migrate more layers than when Y is present. In fact, as the XPS results indicated, Ni content on alumina resulted 2.0 wt%; with Ga-incorporated materials, the Ni content increased as the Ga content also increased (3.3 and 4.7 wt% for AlGa-25 and AlGa-50 respectively. In the case of the materials with yttrium, the mentioned effect was more evident since almost all Ni-impregnated resulted at the surface. With that in mind, we suggested that the better Ni dispersion observed in the Ga-incorporated system is generated by the lower quantity of Ga atoms at the surface. This avoids the nickel migration to the sub-superficial layer and being transformed into $NiAl_2O_4$ spinels. In contrast, Y stabilizes more at the surface, generating a more significant agglomeration of Ni and, consequently, a poorer dispersion. However, we need to consider that dispersion did not decrease to the extreme in which the particles reached the XRD detection limit (≈5 nm) as exhibited by the diffractograms of the Ni/Al-0, Ni/AlGa-x, and Ni/AlY-x samples provided in the supplementary information as Figure S5. These facts are directly linked to the catalytic yield observed in these systems, where the Ni/AlGa-x samples have the highest catalytic activity. Although Y induces more Ni surface species, there seems to be a collective effect in which Ni surface species and the dispersion are essential for getting more active sites for the reaction. The continuous flow evaluation of the activated Ni-based catalysts demonstrated that all samples prepared were active in the water gas shift reaction. From them, the Ni/AlGa-x series was demonstrated to be more active than the Ni/AlY-x counterpart. When comparing the activity of the Ni/AlGa-50 with the Ni/Al-0, the difference was around 50% in all the range of temperatures tested. On the other hand, for the Ni/AlY-x series, the catalyst with 50 wt% of Y_2O_3 resulted in the highest activity in temperatures above 300 °C.

4.2. Activity structure correlation

The evidence obtained from the in-situ catalytic experiments revealed the species formed at the surface in each sample analyzed. The FTIR spectra of the reduced Ni/Al-0 sample exhibited large intensity bands related to the vibration modes of CO, formates, and carbonates bonded to the support (see Fig S6 in the supplementary information). As seen in Section 3.2.2 the adsorption of CO rapidly produced carbonates and formates, although the vibration mode related to the asymmetric carbonates disappeared at above 260°C. At the same time, the υ_{CO2} vibration of formates at 1586 cm^{-1} increased its intensity and then decreased with further increases in temperature. In the presence of water, the band at 3730 cm^{-1} due to M—OH—M was observed to decrease with temperature, as seen in Fig. S7 of the supplementary information. These results and the absence of CO_2 in the in-situ cell effluent allowed us to propose Scheme 2 for the adsorption of CO and water on the Al-0 reduced support.

When temperature increases, the bridged carbonates at 1695 cm^{-1} disappear, and at the same time, the υ_{CO2} and υ_{CH} vibrations of formates increase, reaching a maximum intensity c.a. 260 °C. Meanwhile, the ionic carbonates (CO_3) also increased with the temperature. The FTIR spectra related to the in-situ reaction measurements of Ni/AlGa-25 and Ni/AlY-25 exhibited the same vibrations with small shifts that do not intervene with the assignation of vibrational modes. However, the general profile of the spectra obtained in the three cases was utterly different from each other. On the one hand, the observation of the spectra related to the in-situ WGSR with the Ni/Al-0 catalyst indicates that formates participate actively in the reaction mechanism. However, the evidence obtained from the Ni/AlGa-25 indicates that minor intensity for the formates vibrations led to an increase in reaction rate and higher CO conversion than in their Ni/AlY-25 counterpart. However, a drawback of these Ni/Al-0 and Ni/AlY-25 catalysts is related to the progressive increase in the vibrational mode related to the carbonates in both cases. Coincidently, Finos et al. [61] reported that the presence of Ga on mixed materials with ceria could inhibit the formation of bidentate carbonates, and this effect increased with the increase in gallium oxide content in the sample. The authors stated that the formation of more labile carbonate species could be considered as a signal of an appropriate catalyst for WGSR. Indeed, as mentioned before, the Ni/AlGa-25 catalysts resulted in lower intensity vibration for the carbonates and, at the same time, with high activity. The trend mentioned by Finos et al.[61] also coincides with the trend observed for the catalytic activity at steady state conditions, as seen in Fig. 4, in which the catalysts prepared over the AlGa-x samples displayed the highest activity among materials. Therefore, the interaction of CO and H_2O with the surface of the catalyst could be modulated with the presence of gallium or yttrium. At this point, it is worth mentioning that the surface of the AlY-x samples, with more basicity than the AlGa-x samples, as indicated by the PZC values, have previously demonstrated to form stable carbonates that do not desorb under high-temperature reaction conditions[26]. This could mean that the surface of the AlY-x samples keeps and maintains, to some extent, the CO adsorbed instead of helping to transform it.

In addition, the XPS results indicated that the composition of the support is closely near to the nominal values, as seen in Table 2. However, the 5 wt% of Ni impregnated on the samples varies on the surface materials due to migration phenomenon. Clearly, the Ni/Al-0 loses the large quantity of Ni by migration to the bulk, followed by Ni/AlGa-25 with only 3.3 wt% of Ni at the surface. In fact, we can establish a trend in which the Ni available at the surface of materials follows the next order: Ni/AlY-25>NiAlY-50>Ni/AlGa-50>Ni/AlGa-25>Ni/Al-0. This effect was related to the formation of the subsuperficial spinels of $NiAl_2O_4$ caused by the affinity of the Ni atoms to the tetrahedral sites free of Al^{3+} cation. Table 3 supports this assumption since the deconvolution of the spectra indicated that $NiAl_2O_4$ species are present in all catalysts. These values presented in Table 3 could be combined with the atomic weight % observed in all samples (Table 2) to provide an adequate trend about the real Ni^0 obtained in each sample. Following this idea, multiplying the Ni^0 % of species by the Ni wt% at the surface leads to the total Ni^0 per gram of catalysts for each sample. The values obtained resulted as follows: 5 mg, 9 mg, 17 mg, 24 mg, and 11 mg for the Ni/Al-0, Ni/AlGa-25, Ni/AlGa-50, Ni/AlY-25, and Ni/AlY-50 samples, respectively. From these values, it can be assumed that the more active catalysts would be the Ni/AlY-25 since this sample presented the highest quantity of Ni^0 on the surface among the materials.

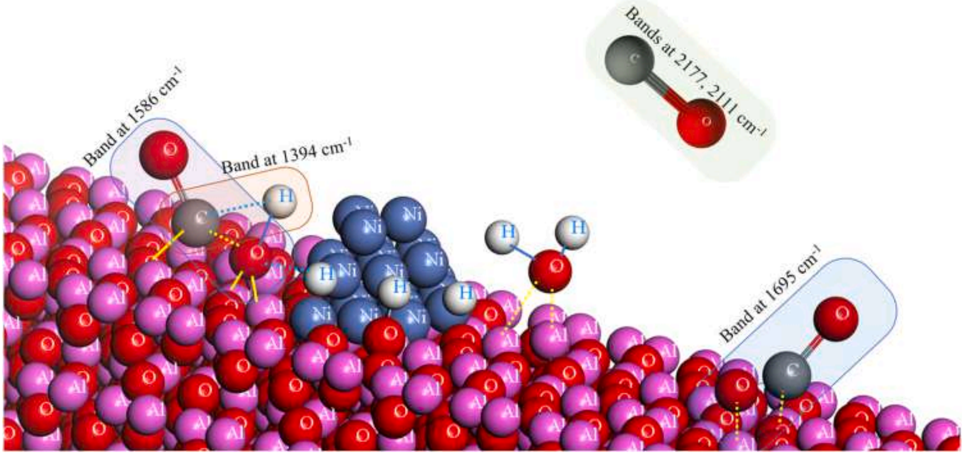

Scheme 2. Simulated model for the adsorption of CO and H_2O molecules over the surface of reduced Ni/Al-0 catalyst (atoms are not at scale), dashed lines indicate the interaction between atoms.

Nevertheless, we need to remember that the catalytically active metal atoms for the WGSR are considered only those located at the periphery of the nanoparticles [7,62] Therefore, the dispersion of nickel over the surface of the supports also plays an essential role in the catalytic activity. Recently, some of us reported that noble metal interacts with AlGa-25 support at different degrees, impacting their dispersion and generating metallic/oxide nanoparticles with different average sizes regardless of the quantity of impregnated metals being the same in all cases [7]. Nevertheless, the authors showed that the sample with the smallest average particle size was not the most active catalyst among the studied materials. In this case, we observed larger Ni particles in the AlGa-50 and AlY-50 than in the AlGa-25 and AlY-25 by the TEM measurement; coincidently, the activity was higher in the two first samples. Another fact that needs to be mentioned is that Ni is well known to form some methane under WGSR conditions, which reduces its efficiency despite the fact that this secondary product could also be used as energy source material [63]. Besides, the main objective of the WGS is hydrogen production; methane must be minimized in the reactor effluent. In this direction, the role of Ni in the WGSR is to adsorb CO and transform it into CO_2 [64]. The observation of nickel carbonyls from 2100 cm^{-1} to 2050 cm^{-1} in the FTIR measurements presented in Section 3.2.2 indicates that the Ni-support interphase is adsorbing CO. With the presence of other nickel nanoparticles in the vicinity, the formation of CO_2 and H_2 is straightforward [63]. However, in these circumstances, formates observed only would be spectators during the reaction of carbonyls [65]. Additionally, literature typically relates the adsorption of CO directly over the Ni^0 species with these vibrational modes [66,67]. We observed in Ni/Al-0 and Ni/AlY-25 samples that the presence of this species depends on temperature, first increasing and then decreasing with the increase in conversion (see Fig. S3 in the supplementary information), avoiding methane formation. Therefore, the WGSR products could be the result of the carbonyl mechanism at low temperatures ($<$ 300 °C) and the formate mechanism at high temperatures ($>$ 300 °C). Further research on DFT calculations is underway to shed light on the mechanism occurring over our Ni-based materials. Finally, we did not observe the presence of methane in the reactor effluents, indicating that these supports could act like methane suppressors under our reaction conditions. Other authors also reported the low production of methane using Ni-based catalysts under WGS reactions [68–70]. Specially Gan at al. proposed that Ni with low coordination number are shown to be the barrier for C–O scission, preventing methane formation as in our case [71]. Finally, we could propose a theoretical study approach considering the Ni adsorption sites on the Ni(111) and Ni(211) surfaces to fully explain our results, as indicated by Yin et al. [72]

5. Conclusions

Nanoscale materials of mixed oxide Al_2O_3 - Ga_2O_3 and Al_2O_3-Y_2O_3, as suitable supports for WGSR Ni catalysts, have been obtained by using a hydrothermal synthesis in the presence of Triton −100 surfactant. Incorporating the two oxides into the alumina structure was complete for the 25 wt% loading. Both alumina oxide promoters induced an enhancement of the WGS catalytic activity, with a more significant effect observed in the Ga-containing catalysts. According to the structural and surface characterization results, Ga and Y modulated the interaction between nickel and Al_2O_3, affecting the surface amount and the sizes of the nickel particles. These two properties determined the number of nickel atoms at the nickel-support border considered the active sites in the WGS reaction. As derived from the in situ FTIR investigation, Ga and Y inhibited the formation of nickel carbonyls, which are considered precursors to the undesired methane formation. The presence of Ga(III) and Y(III) may decrease the surface basicity, decreasing the adsorption of CO and CO_2, resulting in weaker absorption bands. The variation of the formate-related peaks with temperature suggests the involvement of the formate species as intermediates in the reaction mechanism. Further research on DFT calculations is underway to shed light on the exact mechanism occurring over our Ni-based materials.

CRediT authorship contribution statement

R. Ponce-Pérez: Software, Resources, Investigation. **J. Guerrero-Sanchez:** Software, Resources, Investigation. **J.G. Pacheco-Sosa:** Validation, Supervision. **Jorge Noé Díaz de León:** Writing – review & editing, Supervision, Resources, Formal analysis, Conceptualization. **A. M. Venezia:** Validation, Supervision. **S. Jimenez-Lam:** Investigation. **M.C. Ortiz-Domínguez:** Writing – original draft, Investigation, Data curation. **A. Solis-García:** Investigation, Formal analysis. **S. Fuentes-Moyado:** Supervision, Conceptualization.

Declaration of Competing Interest

The authors declare that they have no known competing financial interests or personal relationships that could have appeared to influence the work reported in this paper.

Data availability

Data will be made available on request.

Acknowledgments

The authors want to recognize the financial support provided by DGAPA-PAPIIT IA-100322. COD wants to thank the Ph.D. scholarship provided by CONAHCyT. We thank also thank DGAPA-UNAM projects IG101124, IA100624, and IN101523 for partial financial support. Calculations were performed in the DGTIC-UNAM Supercomputing Center projects LANCAD-UNAM-DGTIC-368, and LANCAD-UNAM-DGTIC-422. Finally, we want to recognize E. Aparicio, I. Gradilla, D. Dominguez, F. Ruiz, E. Flores, J.A. Díaz and P. Casillas for their expert technical assistance.

Appendix A. Supporting information

Supplementary data associated with this article can be found in the online version at doi:10.1016/j.nanoso.2024.101165.

References

[1] T. Shao, L. Cao, L. Li, Y. Su, B. Hou, J. Lin, X. Wang, A noble-metal-free catalyst with MoC nanorod for low-temperature water gas shift reaction, Chem. Eng. J. 485 (2024) 149967, https://doi.org/10.1016/j.cej.2024.149967.
[2] D.C. Grenoble, M.M. Estadt, D.F. Ollis, The chemistry and catalysis of the water gas shift reaction, J. Catal. 67 (1981) 90–102.
[3] S. Saeidi, F. Fazlollahi, S. Najari, D. Iranshahi, J.J. Klemeš, L.L. Baxter, Hydrogen production: perspectives, separation with special emphasis on kinetics of WGS reaction: a state-of-the-art review, J. Ind. Eng. Chem. 49 (2017) 1–25, https://doi.org/10.1016/j.jiec.2016.12.003.
[4] D.S. Newsome, The water-gas shift reaction, Catal. Rev. 21 (1980) 275–318, https://doi.org/10.1080/03602458008067535.
[5] C. Ratnasamy, J. Wagner, Water gas shift catalysis, Catal. Rev. Sci. Eng. 51 (2009) 325–440, https://doi.org/10.1080/01614940903048661.
[6] A.A. Phatak, N. Koryabkina, S. Rai, J.L. Ratts, W. Ruettinger, R.J. Farrauto, G. E. Blau, W.N. Delgass, F.H. Ribeiro, Kinetics of the water-gas shift reaction on Pt catalysts supported on alumina and ceria, Catal. Today 123 (2007) 224–234, https://doi.org/10.1016/j.cattod.2007.02.031.
[7] J.N. Díaz de León, S. Loera-Serna, T.A.A. Zepeda, D. Domínguez, B. Pawelec, A.M. M. Venezia, S. Fuentes-Moyado, Noble metals supported on binary γ-Al2O3-α-Ga2O3 oxide as potential low-temperature water-gas shift catalysts, Fuel 266 (2020) 117031, https://doi.org/10.1016/j.fuel.2020.117031.
[8] C. Wheeler, A. Jhalani, E.J. Klein, S. Tummala, L.D. Schmidt, The water-gas-shift reaction at short contact times, J. Catal. 223 (2004) 191–199, https://doi.org/10.1016/j.jcat.2004.01.002.
[9] T.R. Reina, S. Ivanova, M.A. Centeno, J.A. Odriozola, The role of Au, Cu & CeO2 and their interactions for an enhanced WGS performance, Appl. Catal. B 187 (2016) 98–107, https://doi.org/10.1016/j.apcatb.2016.01.031.
[10] J.L. Santos, T.R. Reina, S. Ivanova, M.A. Centeno, J.A. Odriozola, Gold promoted Cu/ZnO/Al 2 O 3 catalysts prepared from hydrotalcite precursors: advanced materials for the WGS reaction, Appl. Catal. B 201 (2017) 310–317, https://doi.org/10.1016/j.apcatb.2016.08.017.
[11] W. Benzinger, E. Daymo, M. Hettel, L. Maier, C. Antinori, P. Pfeifer, O. Deutschmann, Reverse water gas shift (RWGS) over Ni – Spatially-resolved measurements and simulations, Chem. Eng. J. 362 (2019) 430–441, https://doi.org/10.1016/j.cej.2019.01.038.
[12] L. Foppa, T. Margossian, S.M. Kim, C. Müller, C. Copéret, K. Larmier, A. Comas-Vives, Contrasting the role of Ni/Al2O3 interfaces in water-gas shift and dry reforming of methane, J. Am. Chem. Soc. 139 (2017) 17128–17139, https://doi.org/10.1021/jacs.7b08984.
[13] M. Flytzani-Stephanopoulos, Gold atoms stabilized on various supports catalyze the water–gas shift reaction, Acc. Chem. Res 47 (2014) 783–792, https://doi.org/10.1021/ar4001845.
[14] S.Y. Choung, M. Ferrandon, T. Krause, Pt-Re bimetallic supported on CeO2-ZrO2 mixed oxides as water-gas shift catalysts, Catal. Today 99 (2005) 257–262, https://doi.org/10.1016/j.cattod.2004.10.002.
[15] Q. Fu, A. Weber, M. Flytzani-Stephanopoulos, Nanostructured Au-CeO2 catalysts for low-temperature water-gas shift, Catal. Lett. 77 (2001) 87–95, https://doi.org/10.1023/A:1012666128812.
[16] E.M. Köck, M. Kogler, T. Bielz, B. Klötzer, S. Penner, In situ FT-IR spectroscopic study of CO2 and CO adsorption on Y2O3, ZrO2, and yttria-stabilized ZrO 2, J. Phys. Chem. C. 117 (2013) 17666–17673, https://doi.org/10.1021/jp405625x.
[17] J. Wang, G. Li, Z. Li, C. Tang, Z. Feng, H. An, H. Liu, T. Liu, C. Li, A highly selective and stable ZnO-ZrO2 solid solution catalyst for CO2 hydrogenation to methanol, Sci. Adv. 3 (2017) 1–11, https://doi.org/10.1126/sciadv.1701290.
[18] C.I. Vignatti, M.S. Avila, C.R. Apesteguía, T.F. Garetto, Study of the water-gas shift reaction over Pt supported on CeO 2-ZrO2 mixed oxides, Catal. Today 171 (2011) 297–303, https://doi.org/10.1016/j.cattod.2010.12.041.
[19] C. Li, K. Sivaranjani, J.M. Kim, Synthesis of alkali promoted mesoporous, nanocrystalline Pd/TiO2 catalyst for water gas shift reaction, Catal. Today 265 (2016) 45–51, https://doi.org/10.1016/j.cattod.2015.08.028.
[20] L. Barrio, G. Zhou, I.D. González, M. Estrella, J. Hanson, J.A. Rodriguez, R. M. Navarro, J.L.G. Fierro, In situ characterization of Pt catalysts supported on ceria modified TiO 2 for the WGS reaction: influence of ceria loading, Phys. Chem. Chem. Phys. 14 (2012) 2192–2202, https://doi.org/10.1039/c1cp22509j.
[21] A.R. Kim, B. Lee, M.J. Park, D.J. Moon, J.W. Bae, Catalytic performance on CuO-Cr 2 O 3 -Ga 2 O 3 mixed oxides for water gas shift reaction: effects of Ga/Cr molar ratio, Catal. Commun. 19 (2012) 66–69, https://doi.org/10.1016/j.catcom.2011.12.023.
[22] C. Sener, T.S. Wesley, A.C. Alba-Rubio, M.D. Kumbhalkar, S.H. Hakim, F. H. Ribeiro, J.T. Miller, J.A. Dumesic, PtMo bimetallic catalysts synthesized by controlled surface reactions for water gas shift, ACS Catal. 6 (2016) 1334–1344, https://doi.org/10.1021/acscatal.5b02028.
[23] R.K. Chowdari, J.N. Díaz de León, S. Fuentes-Moyado, Template-free, facile synthesis of nickel promoted multi-walled MoS2 & nano-bricks containing hierarchical MoS2 nanotubes from the bulk NiMo oxide, Appl. Catal. B 298 (2021) 120617, https://doi.org/10.1016/j.apcatb.2021.120617.
[24] M.A. Guzmán-Cruz, C. Ramesh-Kumar, M. Acosta-Alejandro, D.M. Frías-Márquez, D. Domiguez, T.A. Zepeda, S. Fuentes-Moyado, J.N. Díaz de León, Synthesis of aluminium doped Na-titanate nanorods and its application as potential CO2 hydrogenation catalysts, Catal. Lett. 149 (2019) 3361–3369, https://doi.org/10.1007/s10562-019-02902-8.
[25] J.N. Díaz de León, J. Rojas, D. Dominguez, Y. Esqueda-Barrón, J.M. Romo-Herrera, S. Fuentes-Moyado, The effect of shape and size of 1D and 0D titanium oxide nanorods in the photocatalytic degradation of red amaranth toxic dye, Nano Struct. Nano Objects 26 (2021) 100738, https://doi.org/10.1016/j.nanoso.2021.100738.
[26] E.M. Mendoza-Núñez, A. Solis-García, C. Ortiz-Domínguez, C.E. Soto-Arteaga, D. Domínguez, O.E. Contreras, S. Fuentes-Moyado, J.N. Díaz de León, Insight into alcohol transformation over binary Al2O3-Y2O3 mixed oxide nanoparticles, Appl. Catal. B (2022) 121567, https://doi.org/10.1016/J.APCATB.2022.121567.
[27] L. Torrente-Murciano, F.R. Garcia-Garcia, Effect of nanostructured support on the WGSR activity of Pt/CeO2 catalysts, Catal. Commun. 71 (2015) 1–6, https://doi.org/10.1016/j.catcom.2015.07.021.
[28] J.N. Díaz de León, Binary g-Al2O3-a-Ga2O3 as supports of NiW catalysts for hydrocarbon sulfur removal, Appl. Catal. B 181 (2016), https://doi.org/10.1016/j.apcatb.2015.08.028.
[29] G. Kresse, J. Furthmiiller, Efficiency of ab-initio total energy calculations for metals and semiconductors using a plane-wave basis set, B ’ (1996).
[30] G. Kresse, J. Hafner, Ab. initio molecular dynamics for liquid metals, n.d.
[31] G. Kresse, J. Furthmü, Efficient iterative schemes for ab initio total-energy calculations using a plane-wave basis set, 1996.
[32] P.E. Blochl, Projector augmented-+rave method, n.d.
[33] G. Kresse, D. Joubert, From ultrasoft pseudopotentials to the projector augmented-wave method, n.d.
[34] J.P. Perdew, K. Burke, M. Ernzerhof, Generalized Gradient Approximation Made Simple, 1996.
[35] H.J. Monkhorst, J.D. Pack, Special points for Brillonin-zone integrations*, 1976.
[36] J. Chen, D. Sharapa, P.N. Plessow, Stability and formation of hydroxylated α-Al2 O3(0001) surfaces at high temperatures, Phys. Rev. Res 4 (2022), https://doi.org/10.1103/PhysRevResearch.4.013232.
[37] E.M. Mendoza-Núñez, A. Solis-García, C. Ortiz-Domínguez, C.E. Soto-Arteaga, D. Domínguez, O.E. Contreras, S. Fuentes-Moyado, J.N. Díaz de León, Insight into alcohol transformation over binary Al2O3-Y2O3 mixed oxide nanoparticles, Appl. Catal. B 315 (2022), https://doi.org/10.1016/J.APCATB.2022.121567.
[38] J.N. Díaz de León, Binary γ-Al2O3-α-Ga2O3 as supports of NiW catalysts for hydrocarbon sulfur removal, Appl. Catal. B 181 (2016) 524–533, https://doi.org/10.1016/j.apcatb.2015.08.028.
[39] A.E. Awadallah, M.S. Mostafa, A.A. Aboul-Enein, S.A. Hanafi, Hydrogen production via methane decomposition over Al2O 3-TiO2 binary oxides supported Ni catalysts: Effect of Ti content on the catalytic efficiency, Fuel 129 (2014) 68–77, https://doi.org/10.1016/j.fuel.2014.03.047.
[40] J.J. Carberry, Chemical and catalytic reaction engineering, New York, 1976.
[41] Y. Li, Q. Fu, M. Flytzani-Stephanopoulos, Low-temperature water-gas shift reaction over Cu- and Ni-loaded cerium oxide catalysts, Appl. Catal. B 27 (2000) 179–191, https://doi.org/10.1016/S0926-3373(00)00147-8.
[42] C. Zhang, P. Li, Z. Xiao, H. Zhang, E. Yuan, J. Gu, J. Wang, G. Li, D. Wang, Tuning the CO2 hydrogenation activity and selectivity by highly dispersed Ni-In intermetallic alloy compounds, ACS Sustain Chem. Eng. 12 (2024) 166–177, https://doi.org/10.1021/acssuschemeng.3c05215.
[43] A. Paredes-Nunez, I. Jbir, D. Bianchi, F.C. Meunier, Spectrum baseline artefacts and correction of gas-phase species signal during diffuse reflectance FT-IR analyses of catalysts at variable temperatures, Appl. Catal. A Gen. 495 (2015) 17–22, https://doi.org/10.1016/j.apcata.2015.01.042.
[44] F. Azzolina-Jury, F. Thibault-Starzyk, Mechanism of low pressure plasma-assisted CO2 hydrogenation over Ni-USY by microsecond time-resolved FTIR spectroscopy, Top. Catal. 60 (2017) 1709–1721, https://doi.org/10.1007/s11244-017-0849-2.
[45] J. Hu, Y. Li, Y. Zhen, M. Chen, H. Wan, In situ FTIR and ex situ XPS/HS-LEIS study of supported Cu/Al2O3 and Cu/ZnO catalysts for CO2 hydrogenation, Chin. J. Catal. 42 (2021) 367–375, https://doi.org/10.1016/S1872-2067(20)63672-5.
[46] K. Föttinger, W. Emhofer, D. Lennon, G. Rupprechter, Adsorption and reaction of CO on (Pd–)Al2O3 and (Pd–)ZrO2: vibrational spectroscopy of carbonate formation, Top. Catal. 60 (2017) 1722–1734, https://doi.org/10.1007/s11244-017-0852-7.
[47] A. Cárdenas-Arenas, A. Quindimil, A. Davó-Quiñonero, E. Bailón-García, D. Lozano-Castelló, U. De-La-Torre, B. Pereda-Ayo, J.A. González-Marcos, J. R. González-Velasco, A. Bueno-López, Isotopic and in situ DRIFTS study of the CO2

methanation mechanism using Ni/CeO2 and Ni/Al2O3 catalysts, Appl. Catal. B 265 (2020), https://doi.org/10.1016/j.apcatb.2019.118538.

[48] E.P. Meshcheryakov, S.I. Reshetnikov, M.P. Sandu, A.S. Knyazev, I.A. Kurzina, Efficient adsorbent-desiccant based on aluminium oxide, Appl. Sci. 11 (2021), https://doi.org/10.3390/app11062457.

[49] K.I. Hadjiivanov, G.N. Vayssilov, Characterization of oxide surfaces and zeolites by carbon monoxide as an IR probe molecule, Adv. Catal. 47 (2002) 307–511, https://doi.org/10.1016/S0360-0564(02)47008-3.

[50] X. Wang, H. Shi, J.H. Kwak, J. Szanyi, Mechanism of CO2 hydrogenation on Pd/Al2O3 catalysts: kinetics and transient DRIFTS-MS studies, ACS Catal. 5 (2015) 6337–6349, https://doi.org/10.1021/acscatal.5b01464.

[51] L. Foppa, T. Margossian, S.M. Kim, C. Müller, C. Copéret, K. Larmier, A. Comas-Vives, Contrasting the role of Ni/Al2O3 interfaces in water-gas shift and dry reforming of methane, J. Am. Chem. Soc. 139 (2017) 17128–17139, https://doi.org/10.1021/jacs.7b08984.

[52] H. Wijnja, C.P. Schulthess, ATR-FTIR and DRIFT spectroscopy of carbonate species at the aged k-Al 2 O 3 /water interface, 1999.

[53] S.E. Collins, M. a Baltanás, A.L. Bonivardi, Infrared spectroscopic study of the carbon dioxide adsorption on the surface of Ga2O3 polymorphs, J. Phys. Chem. B 110 (2006) 5498–5507, https://doi.org/10.1021/jp055594c.

[54] E.M. Köck, M. Kogler, T. Bielz, B. Klötzer, S. Penner, In situ FT-IR spectroscopic study of CO2 and CO adsorption on Y2O3, ZrO2, and yttria-stabilized ZrO 2, J. Phys. Chem. C. 117 (2013) 17666–17673, https://doi.org/10.1021/jp405625x.

[55] H. Topsøe, B.S. Clausen, F.E. Massoth, Hydrotreating catalysis, Catalysis (1996) 1–269, https://doi.org/10.1007/978-3-642-61040-0_1.

[56] M. Iwamoto, M. Horikoshi, R. Hashimoto, K. Shimano, T. Sawaguchi, H. Teduka, M. Matsukata, Higher activity of Ni/γ-Al2O3 over Fe/γ-Al2O3 and Ru/γ-Al2O3 for catalytic ammonia synthesis in nonthermal atmospheric-pressure plasma of N2 and H2, Catalysts 10 (2020) 590, https://doi.org/10.3390/catal10050590.

[57] H. Huang, L. Wang, Y. Cai, C. Zhou, Y. Yuan, X. Zhang, H. Wan, G. Guan, Facile fabrication of urchin-like hollow boehmite and alumina microspheres with a hierarchical structure via Triton X-100 assisted hydrothermal synthesis, CrystEngComm 17 (2015) 1318–1325, https://doi.org/10.1039/c4ce02133a.

[58] M. Abu El-Oyoun, The effect of addition of gallium on the thermal stability and crystallization kinetic parameters of GaxSe100−x glass system, Phys. B Condens Matter 406 (2011) 125–133, https://doi.org/10.1016/J.PHYSB.2010.10.039.

[59] S. Abalı, S. Kılınç, Effects of sintering temperature on the microstructural properties of Al 2O3–Y2O3 powder mixtures, Int. J. Mater. Res. 112 (2021) 430–438, https://doi.org/10.1515/ijmr-2020-8106.

[60] J. Chen, H. Zhu, L. Wang, J. Zhao, S. Guo, Effect of Yttrium Addition on Nonmetallic Inclusions in FeCrAl Alloys, (2023). https://doi.org/10.1002/srin.202300212.

[61] G. Finos, S. Collins, G. Blanco, E. Del Rio, J.M. Cíes, S. Bernal, A. Bonivardi, Infrared spectroscopic study of carbon dioxide adsorption on the surface of cerium-gallium mixed oxides, Catal. Today 180 (2012) 9–18, https://doi.org/10.1016/j.cattod.2011.04.054.

[62] M. Flytzani-Stephanopoulos, Supported metal catalysts at the single-atom limit - a viewpoint, Cuihua Xuebao/, Chin. J. Catal. 38 (2017) 1432–1442, https://doi.org/10.1016/S1872-2067(17)62886-9.

[63] J. Ashok, M.H. Wai, S. Kawi, Nickel-based catalysts for high-temperature water gas shift reaction-methane suppression, ChemCatChem 10 (2018) 3927–3942, https://doi.org/10.1002/cctc.201800031.

[64] J.H. Lin, V.V. Guliants, Hydrogen production through water-gas shift reaction over supported Cu, Ni, and CuNi nanoparticle catalysts prepared from metal colloids, ChemCatChem 4 (2012) 1611–1621, https://doi.org/10.1002/cctc.201100435.

[65] E.T. Saw, U. Oemar, M.L. Ang, H. Kus, S. Kawi, High-temperature water gas shift reaction on Ni-Cu/CeO2 catalysts: effect of ceria nanocrystal size on carboxylate formation, Catal. Sci. Technol. 6 (2016) 5336–5349, https://doi.org/10.1039/c5cy01932j.

[66] R. Belykh, F. Maugé, A. Tsyganenko, Deep insight into CO adsorption on Ni-USY zeolite catalyst by FTIR spectroscopy. Evidence for isotopic isomerism, V. A. Fock (2019), https://doi.org/10.1016/j.apcata.2019.117140.

[67] J. Zarfl, D. Ferri, T.J. Schildhauer, J. Wambach, A. Wokaun, DRIFTS study of a commercial Ni/-Al 2 O 3 CO methanation catalyst, Appl. Catal. A Gen. 495 (2015) 104–114, https://doi.org/10.1016/j.apcata.2015.02.005.

[68] L. Bobrova, D. Andreev, E. Ivanov, N. Mezentseva, M. Simonov, L. Makarshin, A. Gribovskii, V. Sadykov, Water-gas shift reaction over Ni/CeO2 catalysts, Catalysts 7 (2017), https://doi.org/10.3390/catal7100310.

[69] Y.H. Lee, J.Y. Ahn, D.D. Nguyen, S.W. Chang, S.S. Kim, S.M. Lee, Role of oxide support in Ni based catalysts for CO2methanation, RSC Adv. 11 (2021) 17648–17657, https://doi.org/10.1039/d1ra02327f.

[70] E.T. Saw, U. Oemar, X.R. Tan, Y. Du, A. Borgna, K. Hidajat, S. Kawi, Bimetallic Ni-Cu catalyst supported on CeO2 for high-temperature water-gas shift reaction: methane suppression via enhanced CO adsorption, J. Catal. 314 (2014) 32–46, https://doi.org/10.1016/j.jcat.2014.03.015.

[71] L.Y. Gan, R.Y. Tian, X.B. Yang, H.D. Lu, Y.J. Zhao, Catalytic reactivity of CuNi alloys toward H 2O and CO dissociation for an efficient water-gas shift: a DFT study, J. Phys. Chem. C. 116 (2012) 745–752, https://doi.org/10.1021/jp208119x.

[72] P. Yin, Y. Yang, H. Yan, M. Wei, Theoretical Calculations on Metal Catalysts Toward Water-Gas Shift Reaction: a Review, (2023). https://doi.org/10.1002/chem.202203781.